Polarimetric Radar Variables in the Layers of Melting and Dendritic Growth at X Band—Implications for a Nowcasting Strategy in Stratiform Rain

SILKE TRÖMEL[a]

Institute for Geosciences and Meteorology, University of Bonn, Bonn, Germany

ALEXANDER V. RYZHKOV

Cooperative Institute for Mesoscale Meteorological Studies, University of Oklahoma, and NOAA/OAR/National Severe Storms Laboratory, Norman, Oklahoma

BRANDON HICKMAN, KAI MÜHLBAUER,[a] AND CLEMENS SIMMER[a]

Institute for Geosciences and Meteorology, University of Bonn, Bonn, Germany

(Manuscript received 5 March 2019, in final form 5 September 2019)

ABSTRACT

Time series of quasi–vertical profiles (QVPs) from 52 stratiform precipitation events observed with the polarimetric X-band radar in Bonn, Germany (BoXPol), between 2013 and 2016 have been statistically analyzed to infer microphysical processes shaping the dendritic-growth-layer (DGL) and melting-layer (ML) signatures including surface rainfall. Specific differential phase K_{DP} in the ML shows an average correlation of 0.65 with surface rainfall for these cases. Radar reflectivity decreases below the ML by about 2 dB on average while differential reflectivity Z_{DR} is hardly affected, which suggests rain evaporation as the dominating effect. Estimated ice water content or snow water equivalent precipitation rate S in the DGL is correlated with surface rain rates with lead times of 30 min and longer, which opens a pathway for radar-based nowcasting of stratiform precipitation tendencies. Trajectories of snow generated aloft down to the surface are constructed from wind profiles derived both from the nearest radiosounding and radar-based velocity azimuth displays (VAD) to narrow down the location at which the DGL-generated snow reaches the surface as rain. The lagged correlation analysis between K_{DP} in the DGL and reflectivity Z_H at that location demonstrates the superiority of the VAD information. Correlation coefficients up to 0.80 with lead times up to 120 min provide a proof of concept for future nowcasting applications that are based on DGL monitoring. Statistical relations found in our QVP dataset provide a database for estimating intrinsic polarimetric variables from the usual azimuth and elevation scans within and in the vicinity of the ML.

1. Introduction

The benefits of polarimetric weather radars go far beyond the improvement of quantitative precipitation estimation (QPE). Polarimetric observations also provide a wealth of information on precipitation microphysics, which can be exploited to improve also parameterizations of numerical weather prediction models (NWP; e.g., Kumjian et al. 2014; Kumjian and Ryzhkov 2010; Xie et al. 2016; Carlin 2018; Trömel et al. 2018). In particular, the parameterization of ice microphysical processes, which still are not treated adequately in NWP models, may benefit from such observations. In stratiform clouds, the most pronounced polarimetric signatures apparent in vertical profiles are associated with the dendritic growth layer (DGL) and the melting layer (ML); both carry information about key ice microphysical processes such as depositional growth/sublimation, aggregation, riming, and melting.

A generally accepted and evaluated numerical microphysical model explaining the radar characteristics of the ML does not exist yet, most probably because of still missing exhaustive observational statistics

Denotes content that is immediately available upon publication as open access.

[a] Additional affiliation: Laboratory for Clouds and Precipitation Exploration, Geoverbund ABC/J, Bonn, Germany.

Corresponding author: Silke Trömel, silke.troemel@uni-bonn.de

DOI: 10.1175/JAMC-D-19-0056.1

required for a solid characterization of the relationships between polarimetric variables. Melting processes are not well reproduced by bulk microphysical models partly because of the typically missing mixed-phase hydrometeor categories. Also, more sophisticated models with spectral bin microphysics (SBM) that explicitly treat the mixed phase such as, for example, the Weather Research and Forecasting (WRF) Model coupled with the Hebrew University Cloud Model (HUCM) SBM (e.g., Khain et al. 2011, 2012), do not treat melting in a sufficiently realistic way. An exception is the 1D spectral bin model introduced by Ryzhkov et al. (2014), which Trömel et al. (2014) extended by taking into account accretion in order to investigate the information content of the backscatter differential phase δ. Carlin and Ryzhkov (2017, 2019) further included evaporation and sublimation, which led to very realistic profiles of all simulated polarimetric variables in the ML. A detailed evaluation study with observational statistics of polarimetric variables is still in progress.

Forward (observation) radar operators are now commonly used to aid the improvement of microphysical parameterizations in NWP models, because model results thus transferred to virtual observation can be directly compared with real observations (e.g., Trömel et al. 2018). A good model is then expected to reproduce at least the statistical interrelations of polarimetric variables in the vertical profile in general and in the DGL and ML in particular, which is the central focus of this analysis. First, we review existing techniques to retrieve high-quality vertical polarimetric profiles and then summarize applications oriented specifically toward DGL and ML.

a. *Techniques to retrieve polarimetric radar profiles*

Profiles of polarimetric variables that challenge atmospheric models should be vertically highly resolved and take the decreasing values of polarimetric variables such as differential reflectivity Z_{DR} and specific differential phase K_{DP} with increasing elevation angle into account. Wolfensberger et al. (2016) exploit range–height indicator (RHI) scans (scanned elevation angle at constant azimuth angle) at ranges up to 5 km in their ML analysis in order to limit effects of beam broadening and low signal-to-noise ratio. They also discard elevations of 2° and below to avoid ground clutter contamination and elevations at and above 45° to avoid strong negative biases in Z_{DR} and K_{DP}. Schneebeli et al. (2013) make use of all elevations but correct for effects of the viewing geometry; they first regrid the data into a Cartesian coordinate system, extract five equally spaced vertical profiles between 5- and 10-km horizontal distance from each RHI, and derive empirical distribution functions of polarimetric observables above the melting layer.

An alternative are quasi-vertical profiles (QVPs), which are obtained via azimuthal averaging of the data from plan position indicators (PPIs; azimuthal scans at fixed elevation angles) at elevation angles between 10° and 20°. The azimuthal averaging (e.g., over circles of 55- or 110-km diameter at 5- or 10-km height, respectively, when derived from 10° elevation scans) reduces the statistical errors of the radar variables' estimates. The effective vertical resolution of QVPs depends on the radar radial resolution and beamwidth, leading, for example, to about 100 m at 2-km height and 270 m at 5-km height for the polarimetric X-band research radar in Bonn, Germany (BoXPol; Diederich et al. 2015a,b). Kumjian et al. (2013) first used QVPs to identify polarimetric signatures of refreezing in winter storms, and Trömel et al. (2013, 2014) to reliably estimate backscatter differential phase δ within the ML. Ryzhkov et al. (2016) demonstrated the multiple benefits of QVPs including a more reliable detection of microphysical processes. Tobin and Kumjian (2017) modified the QVP technique to better resolve low-level signatures like the refreezing signature; their so-called range-defined QVPs use PPIs at several elevation angles and create inverse-distance-weighted profiles from the different elevation angles within a specified range from the radar location.

b. *Radar observations of the DGL*

The DGL is usually found between −10° and −15°C and plays a fundamental role in ice generation. Even though the Bergeron–Findeisen process may take place within the entire temperature range between −10° and −35°C where supercooled liquid water and ice crystals may coexist, optimal conditions for ice growth are encountered around the −12°C level where the difference between saturation vapor pressures with respect to ice and to water is maximal. Takahashi et al. (1991) let ice crystals grow in a supercooled wind tunnel at temperatures between −3.8° and −22°C and identified a pronounced maxima of the mass growth rate at −15°C where dendrites and hexagonal plates mostly grow and at −6°C where needles is a dominant growing habit. In the DGL, radar observations are mostly marked by 1) a distinct increase of reflectivity Z_H with decreasing height, 2) a maximum of Z_{DR} and K_{DP}, and 3) a minimum of the cross-correlation coefficient ρ_{HV} [see Kennedy and Rutledge (2011), Andrić et al. (2013), Bechini et al. (2013), Williams et al. (2015), and Griffin et al. (2018), among others]. The Z_{DR} usually decreases below the DGL either by aggregation via a decreasing bulk density and increasingly random orientations of the hydrometeors, and/ or by riming, which tends to make ice particles more spherical. At the same time Z_H increases by both processes, while the decreasing bulk density of snowflakes in case of aggregation or decreasing diversity of shapes in case of riming increases ρ_{HV}. Bands of enhanced K_{DP} and strong downward increases of Z_H in this region often precede precipitation intensification at the surface (Bechini et al. 2013; Trömel et al. 2017).

The first systematic QVP-based study of polarimetric DGL signatures is provided by Griffin et al. (2018) for S-band observations from the operational WSR-88D radars in the United States. They examined five winter precipitation events and found a strong anticorrelation between Z_{DR} and K_{DP} magnitudes; that is, larger Z_{DR} occurs with lower K_{DP} and vice versa, and an obvious dependence of the Z_{DR} and K_{DP} magnitudes on the cloud-top temperature (CTT). The highest K_{DP} values have been observed during periods with low Z_{DR} in clouds with CTTs colder than −30°C. The highest Z_{DR} values occurred together with lower K_{DP} values in shallower and thus warmer CTTs between −25° and −10°C. As outlined by Moisseev et al. (2015), K_{DP} bands indicate an increased number concentration of ice crystals, which lead to aggregation. Griffin et al. (2018) hypothesize that ice particles in high concentration seeding the DGL from above have more spherical shapes than locally generated dendrites or hexagonal plates and mask the high Z_{DR} values inherent to the latter. Thus, K_{DP} enhancements near −12°C are more an indicator of "the onset of aggregation, rather than an indicator of dendritic growth." They conclude that the large number concentrations of oblate, relatively dense ice particles required for aggregation and K_{DP} enhancement may result from either seeder–feeder mechanisms more likely in deep clouds or from ice multiplication.

c. Radar observations of the ML

The ML and its polarimetric signatures mirror microphysical processes above (in ice) and below (in rain). Melting enhances Z_H, Z_{DR}, and K_{DP} mainly due to the higher refractive index of water compared to ice, while ρ_{HV} decreases strongly with the increasing particle diversity and resonance effects. The detection and characterization of the ML has been subject of studies for decades (e.g., Smyth and Illingworth 1998; Fabry and Zawadzki 1995; Giangrande et al. 2008; Wolfensberger et al. 2016) motivated by its relevance for quantitative precipitation estimation, hydrometeor classification, and 0°C isotherm retrieval (Baldini and Gorgucci 2006). Fabry and Zawadzki (1995) provide the most cited reference concerning nonpolarimetric ML statistics. Wolfensberger et al. (2016) characterize polarimetric ML signatures in a large dataset of X-band RHI scans in southern France, the Swiss Alps and plateau, and over Iowa (United States) using a new melting-layer detection method.

In our study, we apply the statistical analysis of polarimetric signatures in the DGL by Griffin et al. (2018) in a different climate region (Europe, Germany), for a different radar wavelength (X band), to a much larger sample, and extend this analysis to the melting layer. Further statistical relations found between variables in the melting layer and its surrounding layers provide a database for future polarimetric vertical profiles of reflectivity (VPR) techniques. For the first time, QVPs are used also to quantify polarimetric ML properties and to relate DGL and ML properties to rain and snow estimates with implications for nowcasting. We suggest a path for snow QPE and nowcasting by estimating the ice water content (IWC) or snow water equivalent precipitation rate S in the DGL using K_{DP} and/or Z_{DR} in combination with Z_H—since the bulk of snow is formed in the DGL (Hobbs and Rangno 1985)—and by projecting this estimate down to the surface. This can also be helpful when the estimation of S from radar observations near the surface might be precluded due to much lower magnitudes of K_{DP} and Z_{DR} there with the increasing randomness of orientation and the decrease in snowflake density (Bukovčić et al. 2018; Ryzhkov et al. 2018).

The paper is organized as follows. Section 2 describes the database. Sections 3 and 4 focus on the analysis of polarimetric variables in the DGL and the ML, respectively. Section 5 follows with some applications and implications of the QVP dataset. Section 6 compares for the first time DGL-based rainfall retrievals with rain gauges at the location to which the bulk of snow generated aloft has been advected and thus provides a proof of concept for potential nowcasting applications. Section 7 gives a summary and conclusions.

2. Data

Our analysis is based on observations by BoXPol installed on a 30-m-tall building next to the Institute of Geoscience and Meteorology at the University of Bonn at 50.73°N, 7.07°E and 99.5 m above MSL. For more technical details, see Diederich et al. (2015a). BoXPol is part of the Jülich Observatory for Cloud Evolution currently developing into a Core Facility (JOYCE-CF), which operates, in addition to BoXPol and many other remote sensing instruments, a second polarimetric X-band radar (JuXPol) about 40 km to the northwest at Forschungszentrum Jülich and provides scientists with quality-controlled monitoring data of cloud and precipitation processes (Löhnert et al. 2015). BoXPol typically operates with a maximum range of 100 km and 100-m radial resolution. The 5-min scan repetition schedule includes a volume scan with PPIs at 10 elevations, a birdbath scan (90° elevation), and one RHI oriented toward JuXPol. The Z_H and Z_{DR} are calibrated following Diederich et al. (2015a). The data used in this study have not been corrected for attenuation and differential attenuation, because of still high uncertainties in the required parameters in the ML.

The analysis is based on the 18° elevation PPI scans processed with the QVP method into vertical profiles of the polarimetric variables. Only data with a cross-correlation coefficient ρ_{HV} above 0.7 are used to calculate their azimuthal median at all ranges. For every ray the radial derivative of the differential phase shift Φ_{DP} is calculated with low-noise Lanczos differentiators to estimate specific differential phase K_{DP} (Vulpiani et al. 2012) before calculating its azimuthal median at all ranges. The implementation in the open source library ''wradlib'' (https://wradlib.org; Heistermann et al. 2013) with a window length of 21, corresponding to 2.1-km slant range for BoXPol, is used for the Φ_{DP} processing. The choice of elevation angle 18° is a compromise, which leads to slightly reduced Z_{DR} and K_{DP} from their values at grazing-angle values [see elevation dependence formulas in Griffin et al. (2018)], but still gives usable information on polarimetric variables with about 100- and 270-m vertical resolution at 2- and 5-km height, respectively. Fifty-two stratiform events with time periods between 1 h 25 min and 12 h 35 min—in total, 215 h 20 min—have been observed with BoXPol during 2013–16. The events were subjectively selected on the basis of quick looks of spatially widespread and temporally (>1.5 h) persistent coverages of significant reflectivities Z_H in the BoXPol measurement range. We did not check whether these cases were also related to homogeneous rainfall distributions at rain gauges within the QVP cone during the whole event. The 52 cases have a mean rain rate of only 1.3 mm h^{-1}, with the majority of rain rates varying between 0 and 2.8 mm h^{-1} (10th and 90th percentiles, respectively, Fig. 6, bottom-right panel). Thus, some events did not produce measured rain at the gauges near BoXPol. These weighing-type rain gauge observations, which are also used in section 3 in a comparison with the temporal evolution of DGL signatures and derived snow rates, are provided by the Landesumweltamt Nordrhein-Westfalen (the state agency for environmental issues), the Erftverband (a regional water management authority), and the city of Bonn (see Diederich et al. 2015b for more information).

To account for horizontal advection of snow generated in the DGL while falling (see section 5), we compare the snow flux with the near-surface reflectivities [Z_H(sfc)], obtained from the 1°-elevation PPI scan, at the projected horizontal location. Snow trajectories are estimated via two different pathways: 1) We used the wind profile observed by the nearest radiosounding taken from the University of Wyoming (http://weather.uwyo.edu/upperair/sounding.html) assuming 1 m s^{-1} average terminal velocity of snowflakes. Either the Essen, Germany, radiosounding (51.40°N, 6.96°E) 74.93 km north of BoXPol (usually available at 0000, 1200, and 1800 UTC) or the Idar-Oberstein, Germany, sounding (49.70°N, 7.33°E) 116.18 km south of BoXPol is used depending on event location and time. 2) We also used radar-derived wind profiles derived from velocity azimuth displays (VADs; Browning and Wexler 1968) of each volume scan available every 5 min and calculated the average wind profile (and its variance) for each precipitation event. The height ranges of the DGL and the cloud-top temperature were derived from the temperature profile of the closest radiosounding. For some events, QVPs are complemented with the temperature forecasts of the operational NWP COSMO Model (Consortium for Small-Scale Modeling; Doms and Schättler 2002; Baldauf et al. 2011) used by the German national weather service (Deutscher Wetterdienst).

3. Statistics of polarimetric variables in the dendritic growth layer

We show as an introductory example QVP time series of Z_H, Z_{DR}, ρ_{HV}, and K_{DP} for a rain event that lasted several hours on 7 October 2014 including the isotherms based on the forecast of the COSMO Model (Fig. 1). This rain event exhibits several of typical polarimetric DGL and ML signatures, described in the introduction section. Enhanced Z_{DR} and K_{DP} are observed at temperatures between −10° and −15°C together with stronger vertical downward increases of Z_H and ρ_{HV}. Aggregation and riming reduce Z_{DR} and K_{DP} below the DGL, while Z_H and ρ_{HV} increase accordingly. The Z_H gradient $\beta = \partial Z_H/\partial z$, an indicator for ongoing aggregation and/or riming, is most pronounced at times with high K_{DP} (e.g., around 0300 UTC) and concurrent with surface precipitation enhancement (see stronger Z_H in the column below the ML). Increases in Z_{DR} with time occur at different heights as the concurrent increases in K_{DP}, as also reported by Andrić et al. (2013) and Moisseev et al. (2015). At 0145 UTC, a region of

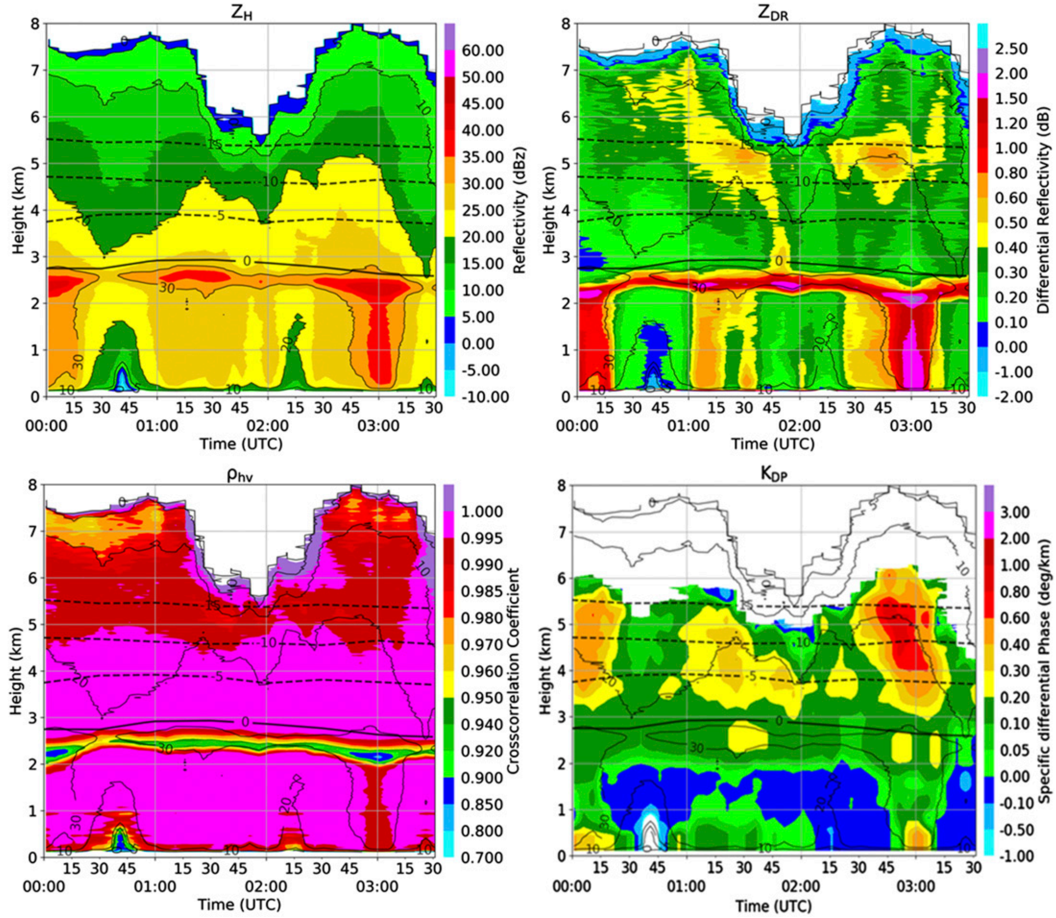

FIG. 1. QVPs of (top left) Z_H, (top right) Z_{DR}, (bottom left) ρ_{HV}, and (bottom right) K_{DP} with black Z_H contour lines (in all panels) observed with the BoXPol radar in Bonn at 18° elevation on 7 Oct 2014 between 0000 and 0330 UTC. The overlaid thick solid and dashed black lines (in all panels) show the 0°, −5°, −10°, and −15°C isotherms from COSMO Model output at the BoXPol location.

increased Z_{DR} extends down to the ML, which hints at prevailing more pristine ice crystals in the column and the absence of aggregation. Throughout the event, the melting layer, indicated by enhanced Z_H and Z_{DR} and a low ρ_{HV}, largely follows the temporal evolution of the 0°C isotherm around 2.7-km height. At 0300 UTC—and also at the very beginning of the observation period around 0000 UTC—a sagging of the melting layer is observed concurrent with a more pronounced Z_{DR} decrease just above the ML compared to other times. These signatures point to either riming accompanied by enhanced fall velocities (e.g., Ryzhkov et al. 2016; Kumjian et al. 2016) or to enhanced aggregation (Carlin and Ryzhkov 2017). Around 0300 UTC, Doppler velocities in the vertical scan (birdbath scan, once every 5 min; not shown) directly above the ML vary between 1.5 and 2 m s^{-1}, which points to relatively light riming on the top of aggregation, which is likely a dominant process responsible for sagging of the melting layer around this time. The Z_H and Z_{DR} enhancements in the ML are correlated, and ρ_{HV} is lowest where riming or strong aggregation takes place.

For the same event we estimated the mass-weighted particle diameter D_m, the number concentration N_t and the ice water content IWC above the ML (Fig. 2) following Ryzhkov et al. (2018):

$$D_m = -0.1 + 2.0\eta \tag{1}$$

with

$$\eta = \left(\frac{z_{DP}}{K_{DP}\lambda}\right)^{1/2}, \tag{2}$$

where λ is the radar wavelength (mm) and $z_{DP} = z_H - z_V$ is the reflectivity difference at orthogonal polarizations expressed in linear scale (mm^6 m^{-3}). The ice water content (g m^{-3}) estimate

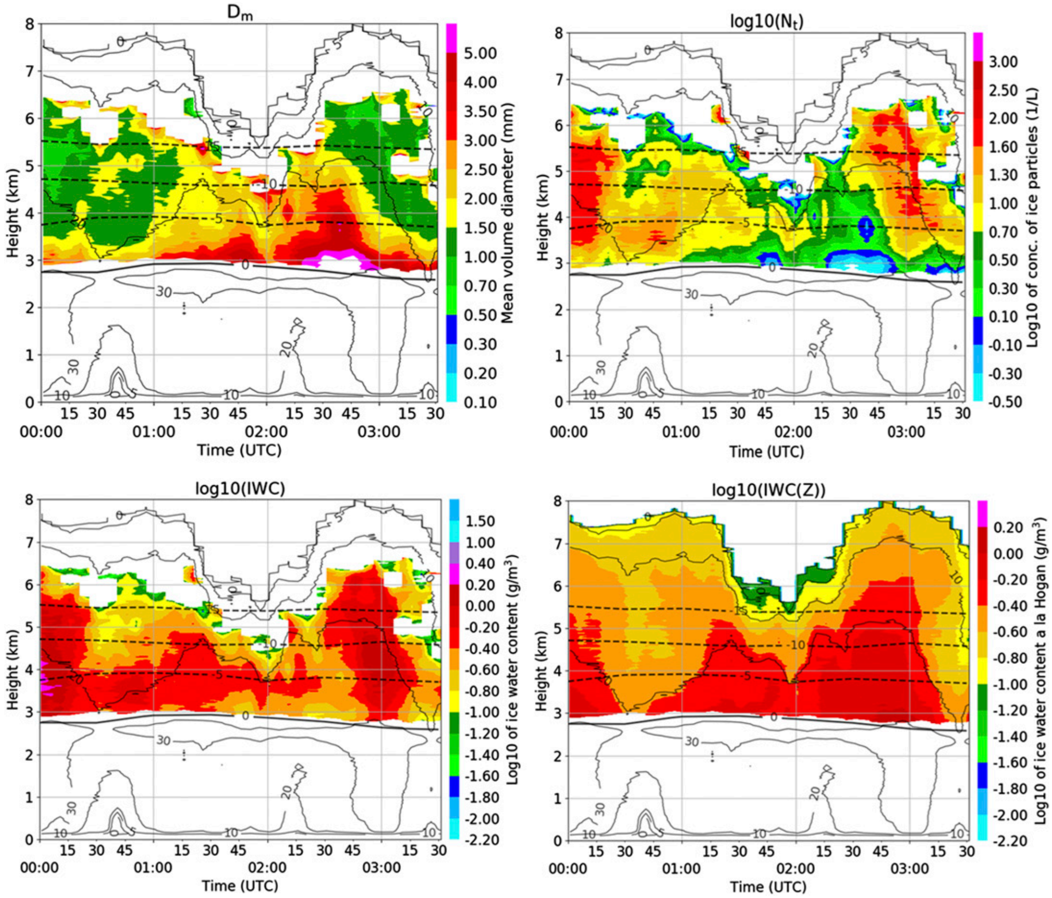

FIG. 2. Polarimetric ice microphysical retrievals of (top left) mean diameter D_m (mm), (top right) total number concentration N_t (L^{-1}), and (bottom left) IWC ($g\,m^{-3}$) as a function of K_{DP} and z_{DP} [Eqs. (1)–(6)] together with black Z_H contour lines (in all panels) observed with the BoXPol radar in Bonn for the event on 7 Oct 2014 shown in Fig. 1. (bottom right) For comparison, the nonpolarimetric retrieval of IWC based on Z_H and temperature [Eq. (7)] is shown. Overlaid thick solid and dashed black lines (in all panels) show the 0°, −5°, −10°, and −15°C isotherms from COSMO Model output at BoXPol location.

$$\mathrm{IWC}(K_{DP}, Z_{dr}) \approx 4.0 \times 10^{-3} \frac{K_{DP}\lambda}{1 - Z_{dr}^{-1}} \tag{3}$$

involves differential reflectivity also expressed in linear scale

$$Z_{dr} = 10^{0.1 Z_{DR}}. \tag{4}$$

The logarithm of the number concentration of ice particles N_t (L^{-1}) is estimated by

$$\log N_t = 0.1 Z_H - 2 \log\gamma - 1.33 \tag{5}$$

with

$$\gamma \approx 0.78\eta^2. \tag{6}$$

The use of the ratio z_{DP}/K_{DP} in these retrievals minimizes effects of the variability of shape and orientation of ice particles, since both variables—z_{DP} and K_{DP}—are proportionally affected by this variability (Ryzhkov et al. 1998). IWC estimated from Z_H alone and the temperature T (°C) via

$$\log \mathrm{IWC}(Z_H) = 0.06 Z_H - 0.0197T - 1.7, \tag{7}$$

following Hogan et al. (2006), is shown for comparison. We believe that the polarimetric estimate is more reasonable, at least where K_{DP} shows significant values, because IWC(Z_H) in Fig. 2 mostly monotonically increases toward lower levels following Z_H, which is not necessarily the case. However, the polarimetric retrievals cannot be applied in regions with low signal-to-noise ratio at far ranges, where noisy and unreliable K_{DP} estimates are repeatedly encountered, resulting in lacking information near the cloud tops.

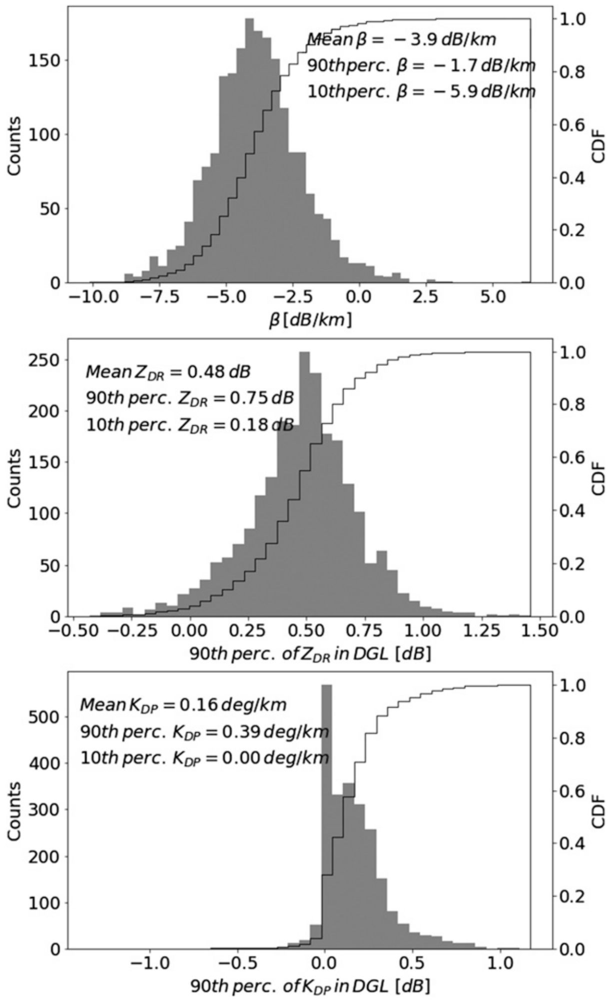

FIG. 3. Histograms (dark-gray bars) and empirical cumulative distribution functions (black lines) of the (top) vertical Z_H gradient β in the 2-km range above the bright band and (middle) Z_{DR}(DGL) and (bottom) K_{DP}(DGL) in the DGL including mean values and 10th and 90th percentiles.

In the following, we present statistics of polarimetric signatures in the dendritic growth layer and below down to the melting layer derived from all 52 cases. The histograms and empirical distribution functions of Z_{DR} and K_{DP} in the DGL, here defined as the layer between the −10°C and −20°C isotherms according to the nearest radiosonde observation, together with the vertical Z_H gradient β of the 2-km-wide layer just above the ML are shown in Fig. 3. For each single profile we define Z_{DR}(DGL) and K_{DP}(DGL) as the 90th percentiles of all Z_{DR} and K_{DP} values as representative maximal values for Z_{DR} and K_{DP} in the DGL following Griffin et al. (2018). The 90th percentile is a good representation of the maximum values encountered in that layer with a low impact of single outliers.

The vertical slope of Z_H above the ML β is computed as

$$\beta = \{Z_H[\mathrm{ML_{top}}(\Phi_{\mathrm{DP}}) + 2\,\mathrm{km}] - Z_H[\mathrm{ML_{top}}(\Phi_{\mathrm{DP}})]\}/2\,\mathrm{km}, \quad (8)$$

where $\mathrm{ML_{top}}(\Phi_{\mathrm{DP}})$ is defined as the height level above the ML excursion of Φ_{DP} caused by backscatter differential phase changes δ, where Φ_{DP} starts increasing with height again. Thus, seen from above $\mathrm{ML_{top}}(\Phi_{\mathrm{DP}})$ is the lowest height level before excursions of the ML in terms of any polarimetric variable start. For the 52 cases, the 10th and 90th percentiles of Z_{DR}(DGL) stay mainly between 0.18 and 0.75 dB and those of K_{DP}(DGL) stay between 0° and 0.39° km^{-1}. The 10th and 90th percentiles of β are −5.9 and −1.7 dB km^{-1}, respectively, which is consistent with observations by Fabry and Zawadzki (1995), Steiner et al. (1995), Vignal and Krajewski (2001), Bellon et al. (2005), and Matrosov et al. (2009).

Our Z_{DR}(DGL) values, which stay below 1.5 dB, are considerably lower than those found in Griffin et al. (2018), Schrom et al. (2015), and Williams et al. (2015), which might be attributed to different radar wavelengths and climatological conditions. Schrom et al. (2015) analyze X-band radar observations of winter storms in northeastern Colorado during the Front Range Orographic Storms (FROST) project and find the largest Z_{DR} values around 3.5–5.5 dB associated with pronounced low-level upslope flows, while the highest K_{DP} values are observed during periods of weaker upslope flow. Griffin et al. (2018) observe Z_{DR}(DGL) values up to 6 dB for CTT between −25° and −10°C in WSR-88D S-band data, whereas at CTTs < −25°C they observed Z_{DR}(DGL) values between 0 and 2 dB. They define CTT as the temperature at the first occurrence of −10 dBZ starting from the top of the QVP. We could not find a cloud-top temperature dependence in our data. Note that our statistics are most likely somewhat negatively biased (below 0.3 dB) because of (differential) attenuation at X band in the ML, for which we did not correct in this study.

A possible climatological explanation for the lower DGL Z_{DR} could be a dryer upper troposphere over central Europe compared to central United States. At temperatures around −12°C, dendrite growth is favored by the largest difference between the saturation vapor pressures over water and over ice. In the radiosoundings for the 52 cases, supersaturation with respect to ice occurs only in about one-half of the cases and stays at moderate levels below 16%. Also, Bechini et al. (2013) find over northwestern Italy mean values of maximal Z_{DR} in the DGL between 0.1 and 1.3 dB in hourly profiles of 54 rainy days of C-band measurements with 90th percentiles between 0.5 and 2.5 dB. Schneebeli et al. (2013) find in the eastern Swiss Alps an average peak value of 0.965 dB with the 20% and 80% quantiles at 0.35 and 1.45 dB, respectively. Thus, these and our study suggest different upper-troposphere climate regimes in central Europe than in the central United States. The study by Vogel and Fabry (2018) performed in Quebec, Canada, also shows Z_{DR}(DGL) mostly below 1.5 dB (their Fig. 7); they find a less pronounced Z_{DR}(DGL) peak in riming cases than in nonriming cases, but the most pronounced peaks for riming cases with bimodal spectra.

Griffin et al. (2018) find for S band that K_{DP} in the DGL varies between 0° and 0.3° km^{-1} for cloud-top temperatures between −30° and −55°C but stays between −0.1° and +0.1° km^{-1} for warmer CTT between −30° and −10°C. Figure 4 (similar to Fig. 9 in Griffin et al. 2018) also suggests an increasing K_{DP} with decreasing CTT in our data; however, it is restricted to more shallow clouds since CTTs do not fall below −40°C. Note that K_{DP} at X band is larger by about a factor of 3 than at S band. Griffin et al. (2018) also find a negative correlation between Z_{DR} and Z_H and a positive correlation between K_{DP} and Z_H in the DGL; that is, higher Z_{DR} occurs within lower Z_H areas, and larger K_{DP} occurs within larger Z_H regions in the DGL. Their negative Z_{DR}–Z_H correlation cannot be confirmed by our data (not shown), probably because of the lack of high Z_{DR}, but the positive correlation between K_{DP} and Z_H is observed (Fig. 4). Probably shallow stratiform clouds never reaching the homogeneous nucleation level are more common over Germany than over the United States.

Figure 5 shows the distribution statistics of the ice microphysical retrievals in the DGL from Eqs. (1)–(6) with D_m(DGL), N_t(DGL), and IWC(DGL) defined as the 90th percentiles at height levels between −10° and −20°C. The DGL ice particle number concentration N_t(DGL) roughly ranges from 3 to 183 L^{-1} (10th and 90th percentiles) with a mean value of 19 L^{-1}. The mass-weighted particle diameter D_m(DGL) mainly varies between 0.8 and 2.8 mm with a mean D_m(DGL) of 1.8 mm. IWC varies between 0.1 and 0.9 g m^{-3} with a mean value of 0.7 g m^{-3}. These ice retrieval statistics are in line with in situ measurements in stratiform clouds with embedded convection in northern China analyzed in Hou et al. (2014): at temperatures around −10°C their maximum IWC stays below 1 g m^{-3} with particle number concentrations N_t below 100 L^{-1} and most particles smaller than 2 mm. In situ measurements in a mesoscale convective system observed during the Midlatitude Continental Convective Clouds Experiment

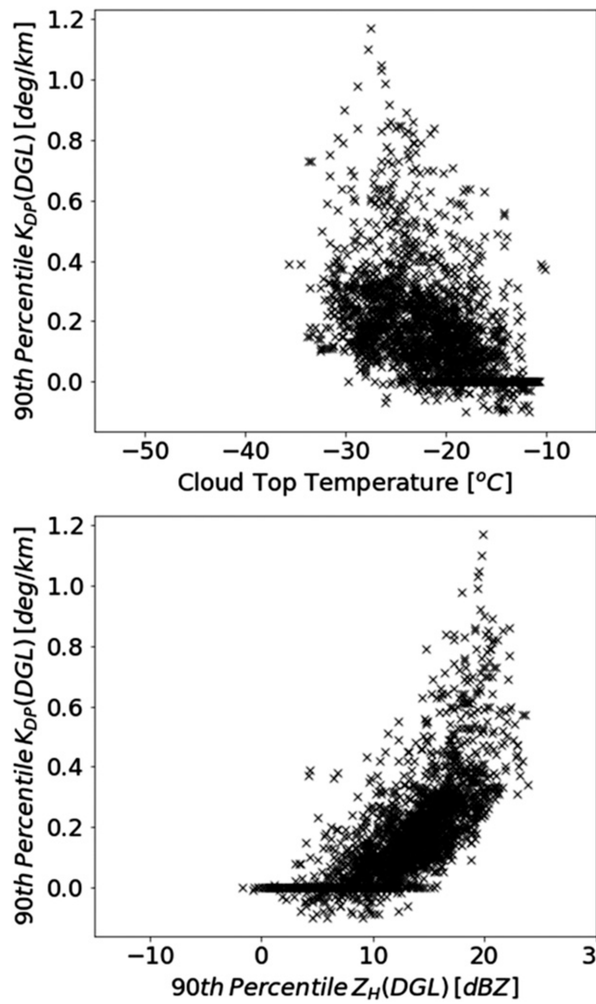

FIG. 4. Relationships between the 90th percentile of K_{DP} in the DGL and (top) cloud-top temperature or (bottom) 90th percentile of Z_H in the DGL from the 52 stratiform events observed for X band over Bonn. The panels are similar to Figs. 9b and 9d of Griffin et al. (2018).

(MC3E) on 20 May 2011, however, indicate smaller D_m values below 1 mm with IWC below 0.5 g m^{-3} and N_t below 50 L^{-1} at temperatures between −10° and −20°C (Ryzhkov et al. 2018). Lower D_m, IWC, and N_t values in a mesoscale convective system in the United States relative to stratiform events in Germany and China appear somewhat unexpected, but the very few in situ measurements in the DGL combined with their inherent uncertainties do not yet permit definitive conclusions on the reliability of ice microphysical retrievals presented in Fig. 5.

According to the relation for the snow water equivalent rate S by Bukovčić et al. (2018),

$$S(\mathrm{IWC}) \approx 3.7 \times \mathrm{IWC}, \tag{9}$$

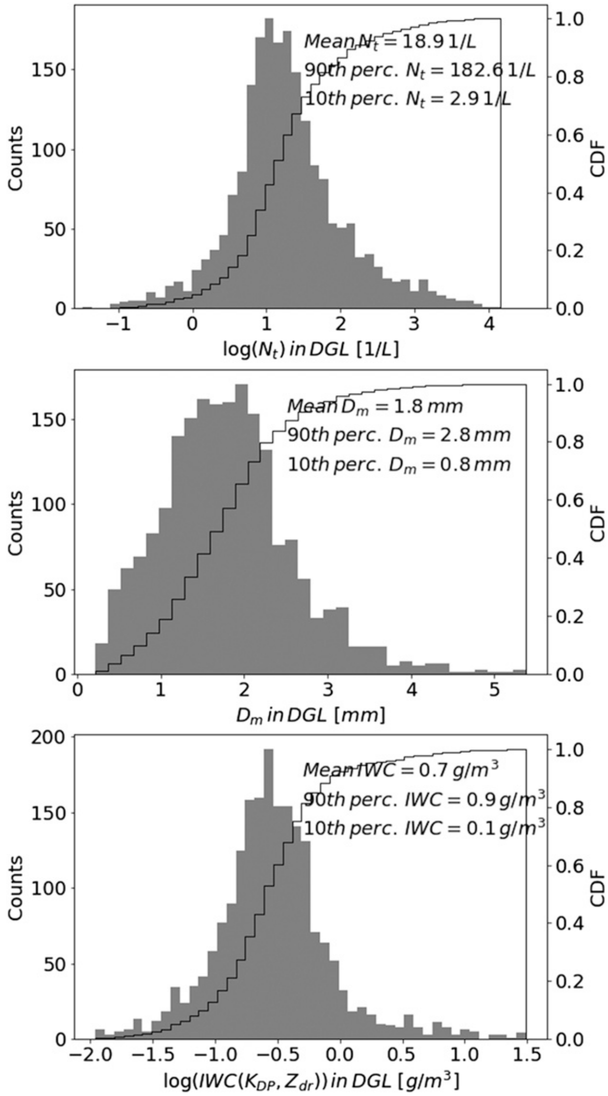

FIG. 5. Histograms (dark-gray bars) and empirical cumulative distribution functions (black lines) of the 90th percentile of (top) N_t (L^{-1}), (middle) D_m (mm), and (bottom) IWC ($g\,m^{-3}$) as a function of K_{DP} and Z_{dr} [Eqs. (1)–(6)] in the DGL (between −10° and −20°C) including respective mean values and 10th and 90th percentiles.

our average IWC in the DGL of $0.7\,g\,m^{-3}$ (Fig. 5) corresponds to $S = 2.6\,mm\,h^{-1}$, while the average rain rate at the surface is $R = 1.3\,mm\,h^{-1}$ (cf. Fig. 6, bottom-right panel). If we correct for evaporation effects below the ML that cause on average a 2.21 dB decrease in Z_H (cf. Fig. 9, described in more detail below), the average rain rate just below the ML is about $1.8\,mm\,h^{-1}$ applying the constant Marshall–Palmer relation. The remaining difference between 2.6 and $1.8\,mm\,h^{-1}$ can be explained by additional sublimation of ice within and above the ML. Nevertheless, this relatively small difference supports the argument that precipitation at the surface (snow or rain) can be at least roughly estimated from polarimetric measurements in the DGL. In section 6 we expand on this by taking trajectories of precipitation from the DGL to the surface into account.

4. Statistics of polarimetric variables in the melting layer

We adapted the ML detection strategy introduced by Wolfensberger et al. (2016) for RHIs to QVPs. Accordingly, ρ_{HV} and Z_H are combined into a single parameter—the melting-layer factor MLF = $Z_H(1 - \rho_{HV})$ with the range of Z_H and ρ_{HV} values first normalized between 0 and 1 to give both variables a similar weight. The maximum and the minimum of the vertical MLF gradient are taken—different from Wolfensberger et al. (2016)—only as a first guess of the top (ML_{top}) and bottom (ML_{bottom}) of the melting layer, respectively, which are then refined to nearby locations in the profile where ρ_{HV} returns to values above 0.97 following Giangrande et al. (2008). The ML depth is then defined as the height difference between ML_{top} and ML_{bottom}; the extremal values of Z_H, Z_{DR}, and ρ_{HV} are determined within this height interval. Besides Wolfensberger et al. (2016) and Giangrande et al. (2008) also other ML-detection schemes exist, for example, by Bandera et al. (1998), White et al. (2002), Matrosov et al. (2007), and Fabry and Zawadzki (1995).

Because of significant contributions of the backscatter differential phase δ to the total differential phase shift $\Phi_{DP,}$ a special processing is required to estimate K_{DP} and δ in the ML, even at X band where δ is low or moderate (Trömel et al. 2014). Trömel et al. (2013) connect values of Φ_{DP} just above and below the ML with a straight line to estimate the vertical K_{DP} profile in the ML. Since excursions of Φ_{DP} by δ may extend to higher altitudes than our ML_{top} estimate based on ρ_{HV}, we connect the straight line starting with Φ_{DP} at ML_{bottom} with Φ_{DP} at the height where it starts increasing again [$ML_{top}(\Phi_{DP})$]. The inherent assumption of that strategy is a constant K_{DP} within the ML. The maximum δ is then estimated as the maximum difference between the Φ_{DP} profile and the straight line. Note that the limited vertical resolution and beam broadening might lead to somewhat lower estimates of maximum Z_H and Z_{DR}, and higher estimates of minimum ρ_{HV} in the ML. Additional variables characterizing the vertical profiles and investigated in the following are Z_H and Z_{DR} in snow directly above the ML and in rain directly below the

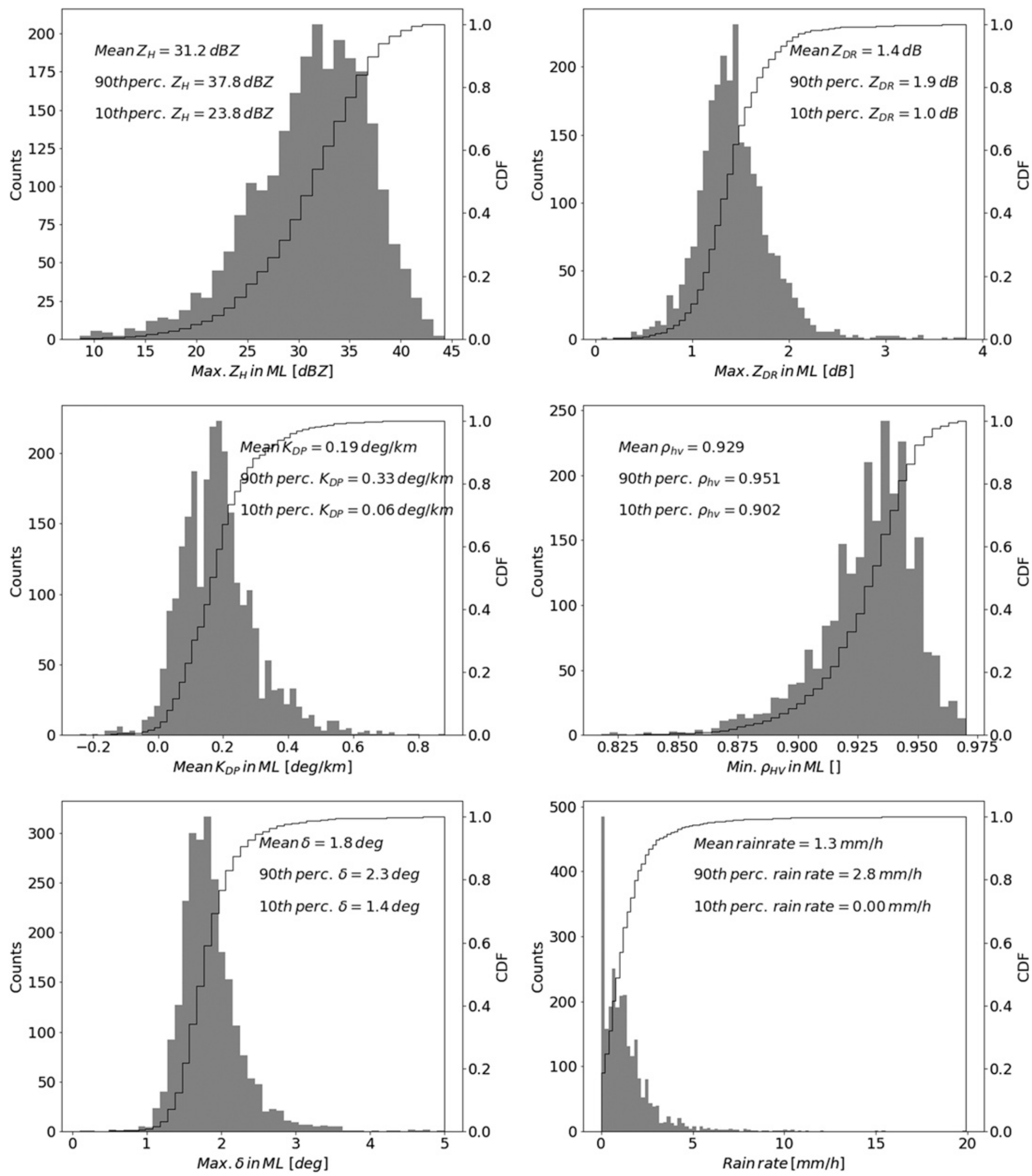

FIG. 6. Histograms (dark-gray bars) and empirical cumulative distribution functions (black lines) of several polarimetric variables in the ML [(top left) maximal Z_H, (top right) maximal Z_{DR}, (middle left) mean K_{DP}, (middle right) minimal ρ_{HV}, and (bottom left) maximal δ] and (bottom right) measured rain rate at the surface. The numbers in the panels indicate arithmetic means and the 10th and 90th percentiles of the respective distribution.

ML, which are again determined at the height levels $ML_{top}(\Phi_{DP})$ and ML_{bottom}, respectively:

$$Z_H(\text{snow}) = Z_H[ML_{\text{top}}(\Phi_{\text{DP}})], \quad (10)$$

$$Z_{\text{DR}}(\text{snow}) = Z_{\text{DR}}[\text{ML}_{\text{top}}(\Phi_{\text{DP}})], \quad (11)$$

$$Z_H(\text{rain}) = Z_H(\text{ML}_{\text{bottom}}), \quad \text{and} \quad (12)$$

$$Z_{\text{DR}}(\text{rain}) = Z_{\text{DR}}(\text{ML}_{\text{bottom}}). \quad (13)$$

Figure 6 shows the histograms and empirical distribution functions of the derived maximum Z_H, Z_{DR}, and δ; minimum ρ_{HV}; and average K_{DP} within the ML derived from the QVP time series for all events. Average values are provided together with the 10th and 90th percentiles for all variables, which enables a direct comparison with the ML statistics provided by Wolfensberger et al. (2016) for Davos (Swiss Alps), Ardèche (southern France), Iowa (midwestern United States), and Payerne (Swiss Plateau; see their Fig. 15 and

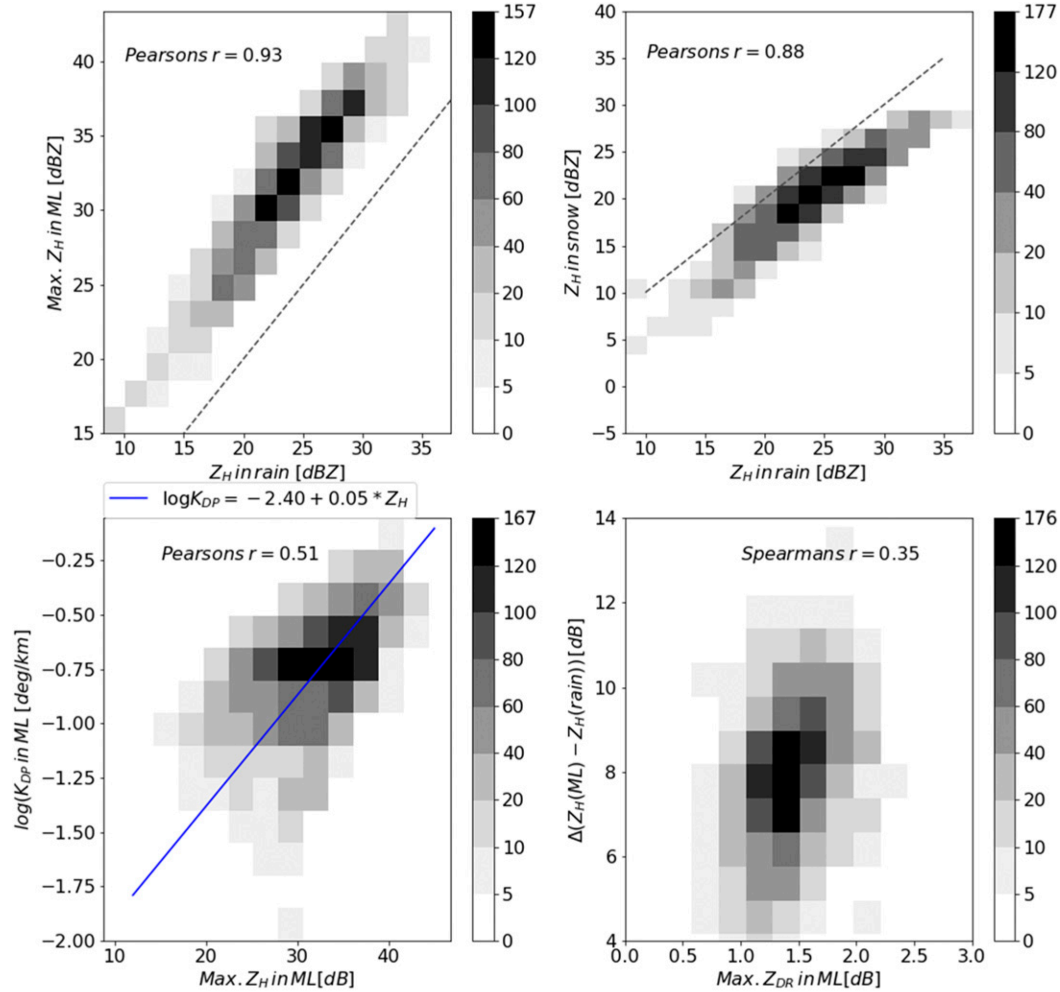

FIG. 7. Scatter density plots and correlations (top left)between maximal Z_H in the ML and Z_H in rain [average difference Z_H(ML) − Z_H(rain) = 7.68 dB], (top right) between Z_H in snow just above the ML and Z_H in rain [average difference Z_H(snow) − Z_H(rain) = −3.9 dB], (bottom left) between log(K_{DP}) in the ML and maximal Z_H in the ML, including the regression line in blue, and (bottom right) between brightband intensity Z_H(ML) − Z_H(rain) and maximal Z_{DR} in ML, i.e., Z_{DR}(ML). Shades of gray indicate the number of observations.

Table 7). Statistics for Bonn are closest to those derived for Davos (Swiss Alps) and to the combined distribution from all four locations. The Davos and the Bonn dataset show similar mean peak Z_H values in the ML of around 31 dBZ. The 10th and 90th percentiles are 22 and 39 dBZ for Davos and 24 and 38 dBZ for Bonn. The minimal ρ_{HV} in Davos, however, reaches lower values with a mean of 0.82 (0.93 for Bonn) and shows a higher variability. Average K_{DP} in Davos and Bonn are very close (0.20° and 0.19° km^{-1}, respectively), however, with a larger spread in the statistics for Davos. The 10th and 90th percentiles are −0.10° and 0.55° km^{-1} for Davos and again narrower with 0.06° and 0.33° km^{-1} for Bonn. Note, however, that Wolfensberger et al. (2016) estimate K_{DP} via Kalman filtering (Grazioli et al. 2014; Schneebeli et al. 2014). The histogram of δ (Fig. 6) is consistent with earlier results by Trömel et al. (2013, 2014). The mean δ is 1.8° for Bonn with the majority of values ranging between 1.4° and 2.3°; these values are generally lower than the ones reported by Griffin et al. (2018) at S band, which might be attributed to stronger resonance scattering effects at X band (Trömel et al. 2014). The scatterplot of $\log_{10}(K_{\mathrm{DP}})$ versus maximal Z_H in the ML (Fig. 7, bottom-left panel) suggests an almost linear relationship between both,

$$\log_{10} K_{\mathrm{DP}}(\mathrm{ML}) = -2.4 + 0.05 Z_H(\mathrm{ML}), \qquad (14)$$

which agrees with simulations with a 1D polarimetric spectral bin model of the ML by Carlin (2018). This consistency between radar observations and simulations indirectly confirms the reliability of the procedure for

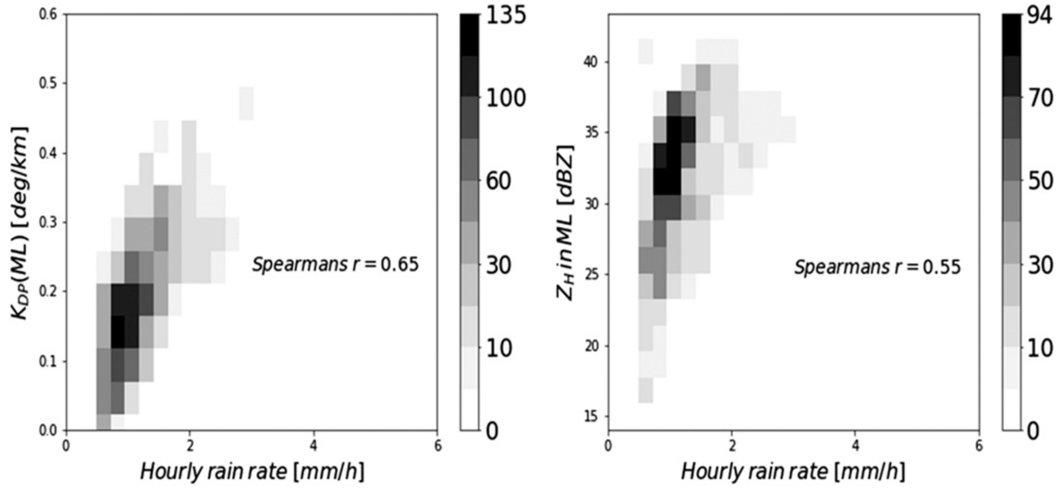

FIG. 8. As in Fig. 7, but for relationships between mean K_{DP} and maximal Z_H in the melting layer monitored with 5-min resolution and measured hourly rain rate (mm h^{-1}) at the surface.

obtaining an average K_{DP} from the QVPs in the ML, which is a key for the evaluation of microphysical models of this region. As demonstrated by Carlin (2018), K_{DP} is proportional to a much-lower-order moment of the size distribution of mixed-phase particles in the ML than Z_H, and it is very closely related to the cooling rate due to the melting of snowflakes; no correlation exists between the cooling rate and Z_H(ML) and Z_{DR}(ML), which are higher moments of the size distribution. K_{DP} is dominated by the more numerous smaller-size particles, which mostly contribute both to total mass and to cooling due to melting and evaporation.

5. Potential applications and implications of the dataset

a. Relations between polarimetric variables in the ML and surface rain rate

Borowska et al. (2011) hint at a promising utilization of K_{DP} within the ML for a better QPE in areas of brightband contamination, which we now can confirm by the relatively strong correlation (Spearmans $r = 0.65$) between K_{DP}(ML) and the measured surface rain rate (Fig. 8, left panel). Similar correlation (Spearmans $r = 0.55$) exists between the maximal Z_H in the ML and the surface rain rate (Fig. 8, right panel). In the following we investigate more closely the relationships between the polarimetric variables within the ML and the ML thickness, the reflectivity in rain just below the ML [Z_H(rain)] and above it [Z_H(snow)], the downward slope of Z_H directly above the ML (β), and the near-surface rain rate to extract the QPE information contained in the ML.

Fabry and Zawadzki (1995) analyze 600 h of vertically pointing X-band radar observations collected at the Marshall Observatory radar site in Canada. According to their statistics, the difference between maximal Z_H in the ML [Z_H(ML)] and Z_H(rain) varies between 5 and 12 dB with increasing differences for Z_H(rain) > 19 dBZ. Our analysis reveals an average difference of 7.7 dB with a standard deviation of 1.9 dB but indicates no significant change/increase for higher dBZ values (Fig. 7, top-left panel). The average difference between reflectivity in the snow just above the ML and the rain below the ML [Z_H(snow) − Z_H(rain)] is −3.9 dB (Fig. 7, top-right panel) in our data with no clear dependence on Z_H(rain), while Fabry and Zawadzki (1995) found almost no difference for Z_H(rain) < 25 dBZ and negative values only for higher Z_H(rain).

Figure 7 (bottom-right panel) reveals a relationship between brightband intensity quantified by Z_H(ML) − Z_H(rain) and the peak Z_{DR} in the ML [Z_{DR}(ML)]. Note that positive correlations between the difference Z_H(ML) − Z_H(rain) and Z_{DR}(ML) are most pronounced for intense bright bands characterized by higher Z_H(ML), which usually indicate large melting snow aggregates developing into large raindrops. Thus, Z_{DR}(ML) may be beneficial to parameterize Z–R relationships. However, snow crystals formed in the DGL and characterized by high Z_{DR} without aggregating as they fall to the melting layer (mostly due to their lower concentration and absence of collisions), may exhibit very high Z_{DR}(ML) (up to 3–4 dB) combined with low Z_H(ML) within the melting layer. Such situations are commonly characterized by very pronounced polarimetric signatures in terms of Z_{DR}(ML)

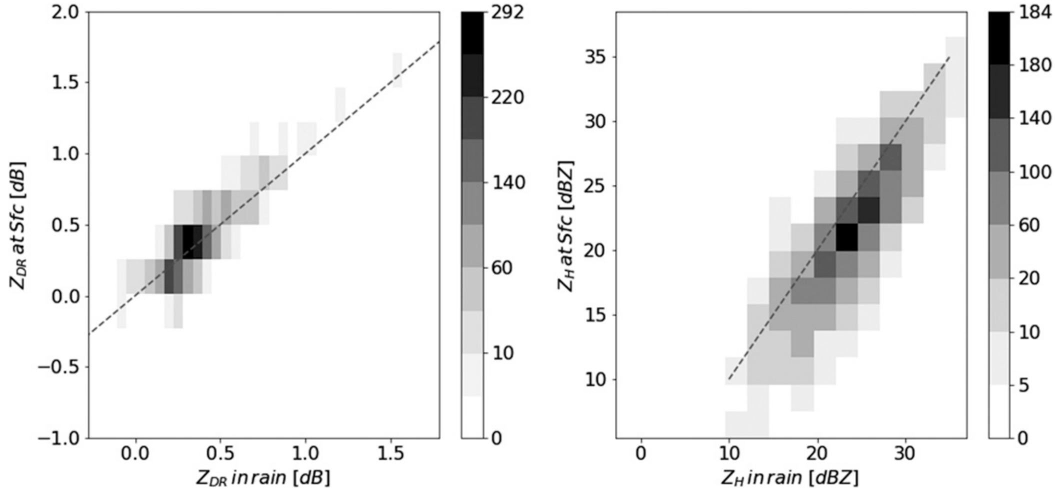

FIG. 9. Relationships between (left) Z_{DR} or (right) Z_H in rain and near the surface. Surface reflectivities Z_H(sfc) and surface differential reflectivities Z_{DR}(sfc) are measured at 750-m slant range (8th radar bin of the 18° elevation scan used for the QVPs). Here, Z_H(rain) and Z_{DR}(rain) refer to the values in rain just below the melting layer. The average difference $Z_{\mathrm{DR}}(\mathrm{rain}) - Z_{\mathrm{DR}}(\mathrm{sfc}) = 0.01$ dB, and $Z_H(\mathrm{rain}) - Z_H(\mathrm{sfc}) = 2.21$ dB.

and ρ_{hv}(ML) and the absence of a reflectivity ''bright band'' (Ryzhkov and Zrnić 2019; see their Figs. 7.19 and 9.11).

b. Impact of evaporation on Z_H and Z_{DR}

Fabry and Zawadzki (1995) find no Z_H(rain) gradient below the ML, whereas the Bonn data reveal an average decrease of Z_H toward the surface of 2.2 dB with a standard deviation of 2.7 dB for average rain-layer depths of 1.9 km (with standard deviation of 0.78 km). The major part of the Z_H decrease can be likely attributed to evaporation (Fig. 9, right panel), which depends on relative humidity and droplet size (smaller drops evaporate faster), while the slowly recovering transmit–receive cell in the radar may only explain a minor contribution. The 3-dB recovery time for BoXPol is estimated to be around 1 μs; taking into account that the measurements defined as surface reflectivity are measured at 750-m slant range and correspond to 5-μs time delay, a residual attenuation close to 2 dB is unlikely. According to the closest radiosoundings the relative humidity at 500-m height varied between 60% and 99% for the 52 events analyzed. A dominance of smaller drops in stratiform rain in Germany or more humid conditions in the lower atmosphere in Canada may explain the deviating results from Fabry and Zawadzki (1995). For a relative humidity of 60% and $Z_{\mathrm{DR}} = 0.27$ dB the expected reflectivity reduction by evaporation within a 2-km-deep rain layer ranges between 2 and 5 dB according to 1D-simulation studies by Kumjian and Ryzhkov (2010) and Xie et al. (2016). In contrast to the impact on Z_H the Bonn data also reveal a negligible impact of evaporation on Z_{DR} (Fig. 9, left panel); the average difference between Z_{DR} in rain (just below the ML) and Z_{DR} at the surface is only 0.01 dB.

c. Correlation analysis toward a polarimetric VPR technique

Since Z_H is significantly higher in the ML than in the rain below, Z_H-based algorithms overestimate rain without appropriate corrections when the radar resolution volume contains melting snow. These algorithms usually underestimate surface rain rates, however, when the radar beam overshoots the ML. In addition, radar beam broadening with distance distorts the vertical profiles of all radar observables and further exacerbates surface rainfall estimation. Thus, a reliable detection and quantification of the bright band including the correlations between different polarimetric variables in the ML is important for the mitigation of brightband contamination in QPE. A possible approach to correct brightband effects on QPE was suggested by Trömel et al. (2017) and requires a profound correlation analysis of polarimetric variables in the intrinsic vertical profiles through the ML. Such correlations can be now obtained from the QVPs, which provide a better height resolution and reduced statistical errors (Fig. 10) when compared with single beams within a PPI scan. The vertical reflectivity gradient above the ML (β) correlates with the peak reflectivity in the ML [Z_H(ML), top-left panel], because β is a measure of aggregation, which increases the particle size − and thus also Z_H − toward the ML. Since stronger reflectivity gradients β result in a stronger underestimation of surface rain rates when corrections

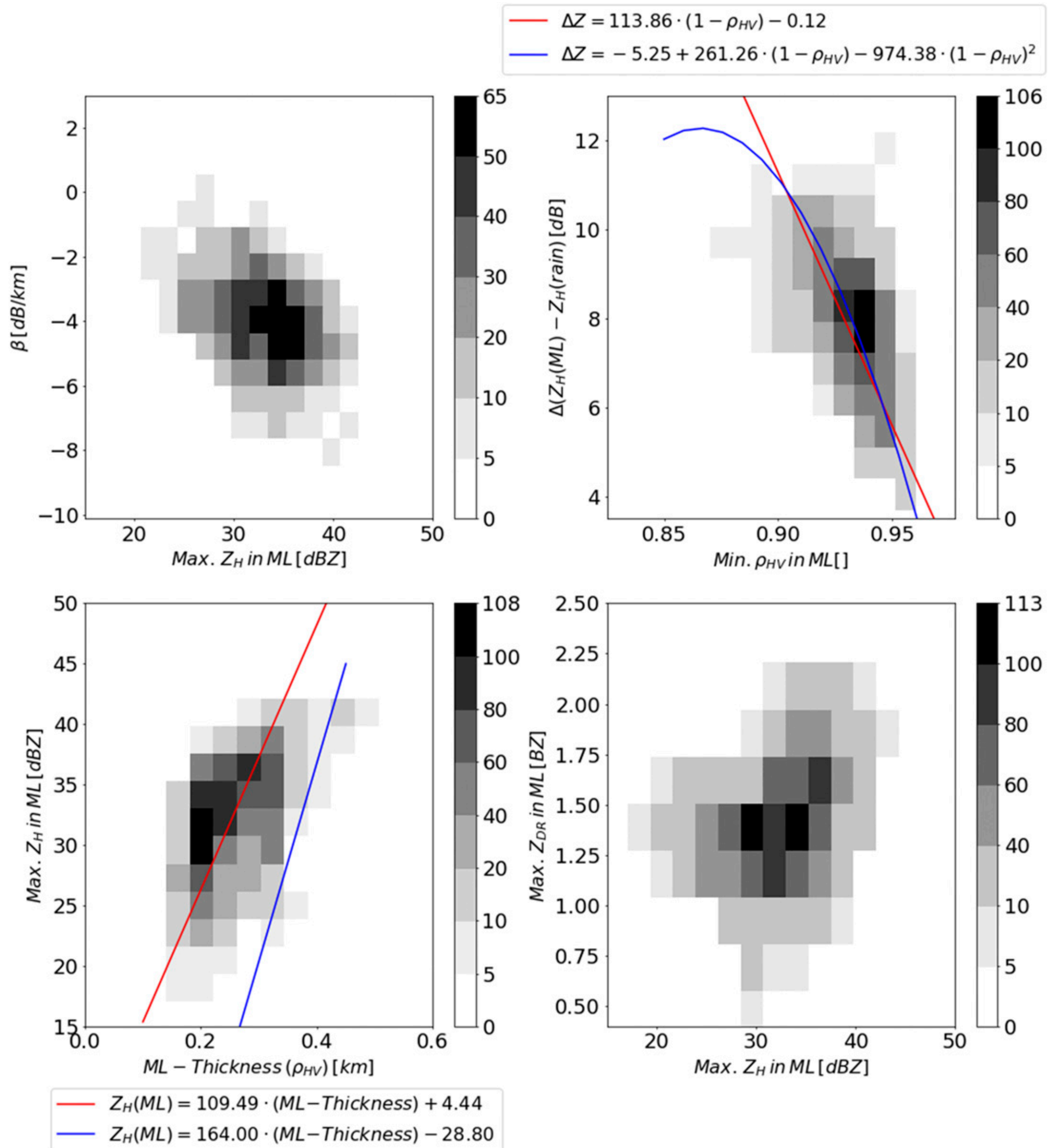

FIG. 10. Similar to Figs. 8 and 9, but showing the relationships (top left) between the vertical gradient in Z_H above the ML (β) and maximal Z_H in the ML and (top right) between brightband intensity Z_H and minimum ρ_{HV} in the melting layer, including linear and quadratic fit (red and blue lines, respectively), (bottom left) between maximal Z_H in the ML and ML thickness, including the linear fit indicated as a red line and comparison with linear fit to statistics by Wolfensberger et al. (2016) indicated as a blue line, and (bottom right) between maximal Z_{DR} and maximal Z_H in the ML.

are not taken into account, β is central for the correction of underestimated Z_H at far ranges [see Fig. 2 in Trömel et al. (2017) for illustration purposes].

Negative correlations exist between the minimum ρ_{HV} in the ML and the brightband intensity $Z_H(\mathrm{ML}) - Z_H(\mathrm{rain})$ (Fig. 10, top-right panel). Both our statistics and those from Wolfensberger et al. (2016) indicate that higher $Z_H(\mathrm{ML})$ also point to deeper MLs (Fig. 10, bottom-left panel), whereas the latter statistics suggests deeper MLs for given $Z_H(\mathrm{ML})$ compared to the Bonn data (cf. the red and blue regression lines in the bottom-left panel). Thus, regional differences must be taken into account. Interestingly, high $Z_{\mathrm{DR}}(\mathrm{ML})$ is found for both high and very small $Z_H(\mathrm{ML})$ (Fig. 10, bottom-right panel, indicates a concave-shaped scatter density plot). As already mentioned before (see section 5a), small $Z_H(\mathrm{ML})$ may occur in the absence of a reflectivity bright band if small nonaggregated ice crystals with very

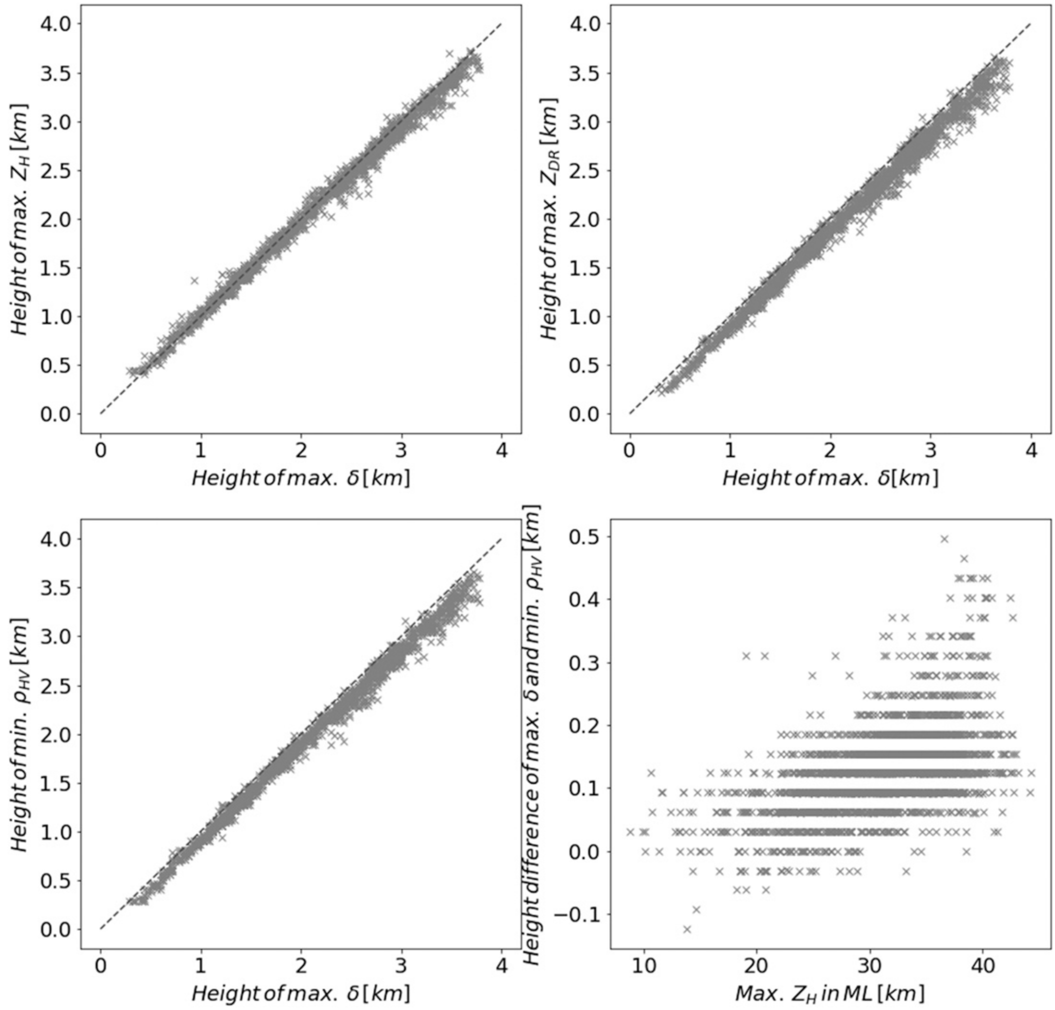

FIG. 11. Relationship between heights of (top left) maximal Z_H and δ, (top right) maximal Z_{DR} and δ, and (bottom left) minimal ρ_{HV} and maximal δ, as well as (bottom right) the height difference between the levels of maximal δ and minimal ρ_{HV} $\{h[\max\delta(\mathrm{ML})] - h[\min\rho_{HV}(\mathrm{ML})]\}$ vs maximal Z_H.

nonspherical shape reach the ML. This nonmonotonic relationship is even more pronounced in the S-band radar data collected in the United States (E. Griffin 2019, personal communication).

Figure 11 puts the results of the study on the relative heights of the extremes in the ML by Trömel et al. (2013, their Fig. 17) on a broader database. Simulations suggest that the height of the peak Z_H is above the ρ_{HV} minimum and the δ maximum, with the latter two at approximately the same height. Our current analysis, however, confirms first observational indications by Trömel et al. (2013): Z_H and δ peak at about the same height with the minimum of ρ_{HV} below at distances increasing up to 500 m with increasing Z_H(ML) (Fig. 11, bottom-right panel). Since the magnitudes of K_{DP} and δ differ considerably, we assume the inexactness of separating a constant average K_{DP} in the ML from total differential phase shift should not significantly affect the estimated height level of the δ peak. Further statistics in different climate regimes are required to clarify whether local microphysical differences are responsible for the differences in the heights of the maxima, or whether a general deficiency in the simulation of the ML in existing cloud models is to blame. For example, Carlin and Ryzhkov (2019) found not only the particle size distribution but also environmental conditions impact height and thickness of the bright band.

Overall, our analysis provides interesting relations between descriptors of the ML and its surrounding layers, which could be exploited to extent the VPR technique (construction of intrinsic reflectivity profiles from observations distorted by brightband effects) with and to polarimetric variables (PVPR). A detailed description and example application are, however, beyond

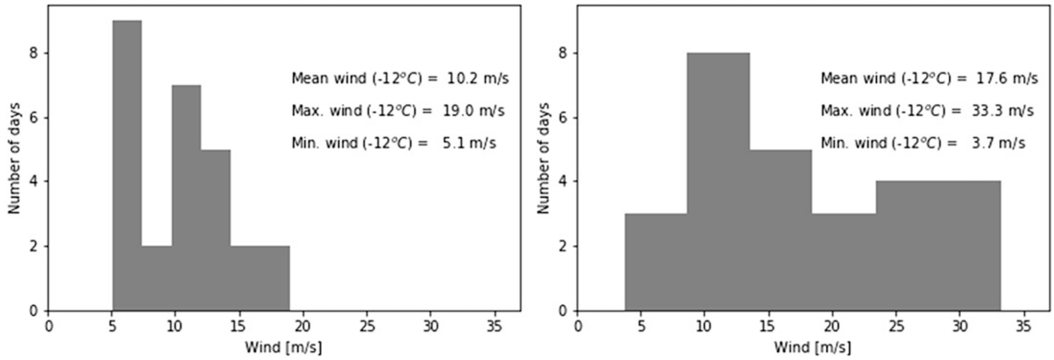

FIG. 12. Empirical distribution of wind speed at −12°C height level based on both the (left) average velocity azimuth displays and (right) nearest radiosounding in space and time of the associated long-lasting events above 3.5 h presented in Table 1.

the scope of this paper and will be a subject of another paper.

6. A pathway for nowcasting

Kennedy and Rutledge (2011) analyze winter storms and linked K_{DP} enhancements aloft with snowfall intensification at the surface taking fall trajectories into account. Bechini et al. (2013) extend their analysis and showed statistical evidence of the relevance of K_{DP} signatures for short-term forecasting regardless of the precipitation type near the surface. They found pronounced correlations between K_{DP} aloft (0.8) and Z_H in rain. Following these findings, we examine correlations of K_{DP} in the DGL [K_{DP}(DGL)] and near-surface Z_H as a proxy for surface precipitation taking estimated fall trajectories into account in our dataset to further explore the prognostic power of K_{DP}.

Given the DGL at about 2 km above the ML and a fall velocity of about 1 m s^{-1} for snowflakes, lead times of more than 30 min can be expected for impacts of DGL processes on precipitation below the ML and thus surface precipitation. Since the bulk of snow precipitation forms within the DGL (e.g., Hobbs and Rangno 1985), it is reasonable to expect that IWC or snow precipitation flux S in the DGL correlates with precipitation intensity at the surface—be it snow or rain—when the falling trajectories are taken into account. Using the measurements at lower heights decreases the potential lead time, and the information content, especially of K_{DP}, is expected to degrade because of the decrease associated with aggregation processes. Trömel et al. (2017) find such correlations for horizontal winds below 10 m s^{-1} up to the −15°C level on 16 November 2014 for lead times of 30 min. In low-wind situations, snowflakes generated in the DGL will mostly stay within the QVP cone (about 70 km in diameter in the DGL) and allow for lagged-correlation analyses using QVPs. For higher winds, however, snowflakes may be advected out of the QVP cone, particularly at lower altitudes. For the 27 long-lasting events with durations above 3.5 h we computed the trajectories of snow from the −12°C height level to the ML height using both direct wind observations from the closest radiosounding and radar-derived velocity azimuth displays (VADs) while assuming 1 m s^{-1} fall velocity for snowflakes. The wind speed in the DGL estimated from the nearest radiosondes varied between 3.7 and 33.4 m s^{-1} with a mean value of 17.6 m s^{-1}, while VAD-derived wind profiles, which provide areal averages over the radar domain, vary between 5.1 and 19.0 m s^{-1} and show a lower average wind speed of 10.2 m s^{-1} (Fig. 12). The estimated trajectories reveal that snow generated in the DGL is advected on average 34 or 30 km off the BoXPol location, when estimated based on radiosondes and VAD, respectively (see Fig. 13 for the distribution of estimated advection distances), which is in line with investigations from Lauri et al. (2012) for the Finnish radar composite indicating distances on the order of tens of kilometers. Table 1 summarizes for the long-lasting events the lagged correlation analysis between K_{DP}(DGL) and Z_H(sfc) with and without taking advection into account, and compares the results based on the different wind information. The correlation analyses without advection are performed from the QVPs only. K_{DP}(DGL)—defined as the 90th percentile of K_{DP} at height levels between −10° and −20°C—is correlated with Z_H at 325 m above the surface for time lags between 0 and 120 min. Maximum values of Spearman's correlation coefficient reaching 0.79 are found for lag times up to 60 min.

In the low-wind case on 16 November 2014 discussed in Trömel et al. (2017, also included in Table 1), snow generated in the DGL reached the ML with a horizontal displacement of only 2 or 6 km with wind information

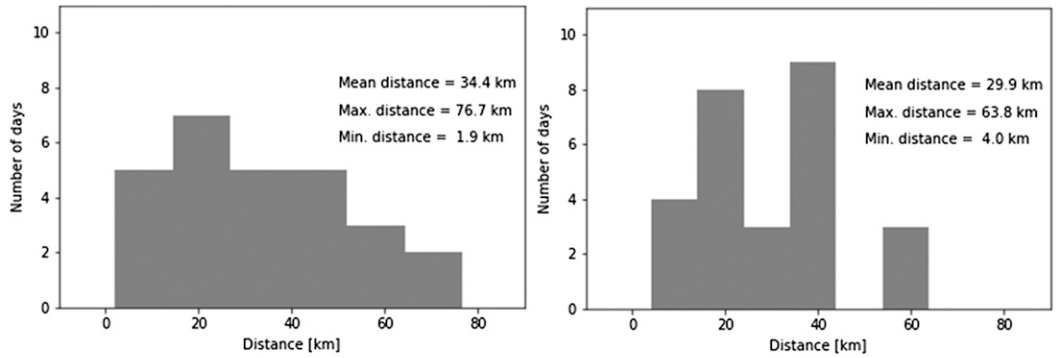

FIG. 13. Empirical distribution of expected distances of snow detected at the BoXPol radar location advected by (left) the wind observed from the closest radiosoundings and (right) the wind derived from velocity azimuth displays (VAD) for the long-lasting events above 3.5 h presented in Table 1.

from the nearest radiosounding or VADs, respectively. Correlations without advection-estimated lags are already significant and are highest ($r = 0.64$) for a lag time of 5 min for this case. We also correlated K_{DP}(DGL) with Z_H from the PPI scan at 1° elevation (averaged over 5° in azimuthal and 2.1 km in radial direction) at the two estimated transections of the trajectories with the ML using radiosoundings and VADs located 2 and 6 km, respectively, from the position of the radar, which results in similar correlation coefficients of 0.66 and 0.67 for 20-min lag time in both cases. When extending, however, the analysis to the 27 selected cases (listed in Table 1), we achieve higher correlations for 19 cases by using the VAD profiles.

In our analysis, one VAD is derived for every volume scan available every 5 min during each precipitation event. The average VAD wind profile of each event listed in Table 1 is used for the trajectory analysis with the variance providing a measure for the uncertainty of the trajectory. Table 1 provides the variance of wind speed and directions during each event averaged along the profiles. Note that the estimated circular variance of wind direction α,

$$\mathrm{var}(\alpha) = 1 - \left[\left(\frac{1}{N}\sum_{i=1}^{N}\sin\alpha_i\right)^2 + \left(\frac{1}{N}\sum_{i=1}^{N}\cos\alpha_i\right)^2\right]^{1/2}, \tag{15}$$

is bounded between 0 and 1. Even though the highest correlations are achieved for the cases with very low circular variance in wind direction, no clear relationship between the Spearman correlation coefficient and the wind variability is visible, most likely due to superposition with other error sources (see section 6 for further discussions). Figure 14 illustrates the comparison of mean radar-derived wind profiles including the temporal variability with the measured wind profile at the nearest radiosounding for the precipitations on 27 February 2015 and 12 April 2013. VAD analyses uncovers higher variability in wind directions during the event on 27 February showing low correlations (about 0.4) between K_{DP} in the DGL and Z_H at the estimated advected surface location while little change in wind direction occurred during the event on 12 April 2013 with high correlation (about 0.8).

For the following figures, always temporally averaged VADs have been used. Figure 15 demonstrates the similarity of the time series of K_{DP}(DGL) and the lagged near-surface Z_H at the advected position (top and middle panel) for the low-wind case on 16 November 2014. We also compare the DGL snow water equivalent precipitation rate S estimated from different IWC retrievals using Eq. (9) with rainfall rates R derived from surface reflectivities Z_H at the estimated location where the bulks of snow generated aloft should reach the surface and with measured rainfall rates from the two nearest rain gauges (Heizkraftwerk and Bad Godesberg Nord) located at 2.11- and 1.38-km distance from the estimated location, respectively. IWC retrievals are based either on K_{DP} and Z_{dr} [Eq. (3)] or on K_{DP} and Z_H in the DGL,

$$\mathrm{IWC}(K_{DP}, Z_H) = 0.32K_{DP}^{0.65}Z_H^{0.28} \quad \text{and} \tag{16}$$

$$\mathrm{IWC}_2(K_{DP}, Z_H) = 0.28K_{DP}^{0.61}Z_H^{0.33} \tag{17}$$

(Bukovčić et al. 2018). For the comparison the local Z_H–R_{Bo} relationship

$$Z_H = 72R_{Bo}^{2.14} \tag{18}$$

for the city of Bonn is used. It showed the best agreement between BoXPol-derived rain rates and the local rain gauge network between May and September 2010

TABLE 1. Dates of case studies with 3 h 30 min observation length and more together with time lag of maximal Spearman correlation coefficients between K_{DP} in the DGL and surface reflectivity Z_H(sfc) at the BoXPol location (r) and the estimated advected locations using sounding (r_s) and VAD information (r_{VAD}), respectively. Based on the VADs calculated for each radar volume available every 5 min., the temporal variances of wind direction [Eq. (15)] and wind speed during each rain event are provided as vertical mean values. Case studies shown in Figs. 15–17 are highlighted in boldface font; the low-wind case also investigated in Trömel et al. (2017) is listed in italics.

Date	Period (h:min)	Without advection: Lag (min)	Without advection: r	Distance$_s$/Distance$_{VAD}$ (km)	With advection, at estimated location: Lag$_s$/Lag$_{VAD}$ (min)	With advection, at estimated location: r_s/r_{VAD}	Variance wind speed ($m^2 s^{-2}$)/direction	Max K_{DP} in DGL (° km^{-1})
12 Apr 2013	**4:05**	**0**	**0.57**	**36.32/23.11**	**50/30**	**0.77/0.80**	**1.03/0.01**	**0.7**
3 Jul 2013	3:55	15	0.65	22.67/20.94	75/70	0.78/0.62	1.01/0.01	0.36
6 May 2014	5:00	5	0.36	39.67/38.95	65/55	0.42/0.27	4.46/0.02	0.98
27 May 2014	4:35	60	0.56	9.63/3.96	20/120	0.49/0.74	0.47/0.15	0.3
8 Jul 2014	5:00	60	0.14	9.49/9.47	45/45	0.43/0.58	0.54/0.06	0.26
9 Jul 2014	12:35	10	0.47	13.55/28.25	45/30	0.45/0.44	3.43/0.10	0.4
26 Aug 2014	6:10	0	0.71	30.85/19.12	55/25	0.64/0.68	1.91/0.07	0.86
7 Oct 2014	**3:30**	**0**	**0.75**	**35.91/41.10**	**55/50**	**0.67/0.75**	**2.29/0.02**	**0.75**
4 Nov 2014	11:05	35	0.33	49.5/23.85	0/50	0.28/0.50	5.55/0.13	0.33
12 Dec 2014	4:35	15	0.36	55.34/35.33	95/35	0.54/0.54	1.41/0.02	0.38
16 Nov 2014	***9:25***	***5***	***0.64***	***1.89/5.89***	***20/20***	***0.66/0.67***	***3.06/0.12***	***0.33***
19 Dec 2014	4:20	0	0.28	59.74/60.59	30/30	0.52/0.40	2.03/0.01	0.23
27 Feb 2015	6:05	0	0.31	25.01/21.0	80/70	0.37/0.38	0.95/0.15	0.3
29 Mar 2015	4:25	15	0.12	76.72/63.82	95/55	0.56/0.48	1.37/0.01	0.3
2 Apr 2015	3:35	60	0.76	50.18/37.96	30/15	0.64/0.76	0.68/0.02	0.37
3 May 2015	4:10	10	0.61	33.97/36.12	70/75	0.56/0.50	1.67/0.03	0.47
22 Jun 2015	12:05	40	0.43	48.90/37.01	0/0	0.57/0.66	2.26/0.02	0.39
17 Aug 2015	5:45	30	0.66	8.57/9.99	60/55	0.60/0.72	0.10/0.03	0.3
27 Aug 2015	9:55	0	0.35	62.62/57.52	50/0	0.56/0.64	4.52/0.04	0.79
1 Sep 2015	6:40	15	0.69	36.69/33.93	35/35	0.55/0.57	2.44/0.12	0.71
16 Sep 2015	4:50	50	0.51	40.49/42.32	35/80	0.46/0.67	4.76/0.03	0.39
22 Sep 2015	3:35	0	0.46	25.17/28.50	100/30	0.41/0.43	1.18/0.03	0.58
19 Nov 2015	4:25	35	0.35	74.87/41.04	50/30	0.28/0.62	3.08/0.04	0.33
8 Dec 2015	3:40	15	0.60	25.08/14.96	120/100	0.76/0.56	0.94/0.01	0.49
11 Dec 2015	4:35	20	0.25	14.55/29.54	5/45	0.48/0.52	3.40/0.01	0.27
16 Dec 2015	4:20	10	0.38	19.52/20.18	60/0	0.11/0.15	0.93/0.04	0.41
2 Jan 2016	5:45	60	0.79	23.21/23.30	115/35	0.46/0.62	1.45/0.02	0.27

(Diederich et al. 2015b). The results are encouraging; that is, the three polarimetric S(IWC) estimates produce very similar results and largely follow the temporal evolution of the $R_{Bo}(Z_H)$-derived rain rates 20 min later. The rain rates measured at the nearest gauges, however, are a bit higher.

Good results are also achieved for the other cases with relatively low winds and advection distances around 10 km and less such as the precipitation events on 27 May 2014, 8 July 2014, or 17 August 2015. The highest correlation, however, is achieved for the event on 12 April 2013 (Fig. 16), which exhibits a pronounced K_{DP} band in the DGL reaching 0.7° km^{-1} (not shown). Without taking advection into account the highest correlation between K_{DP}(DGL) and Z_H(sfc) from the QVPs is observed for a zero lag time with $r = 0.57$. With Z_H near the surface at the estimated arrival location at a distance of 23.11 km (22.25 km in the x direction and 6.23 km in the y direction) from the BoXPol PPI at 1° elevation r is highest (0.80) for a lag time of 30 min. Again, all S(IWC) retrievals match nicely with the observed rain rates estimated from gauges at the corresponding location and the ones derived from the surface reflectivities using Eq. (18). However, the latter two show a bit higher peak values in the second part of the rain event.

Figure 17 illustrates the results for the event observed on 7 October 2014, the QVPs of which are presented in Fig. 1. A good overall agreement between S(IWC) retrievals and the two surface rain rates is achieved except one more pronounced deviation of R_{Bo} to higher rain rates at 0350 UTC. Despite an estimated advection of the snow generated in the DGL 41.10 km away from the QVP center location, K_{DP}(DGL) and Z_H at 325 m with zero lag time from the QVPs show already a high correlation of 0.75. The same correlation is achieved for a lag time of 50 min when advection is taken into account. The high correlations at very different time lags for this

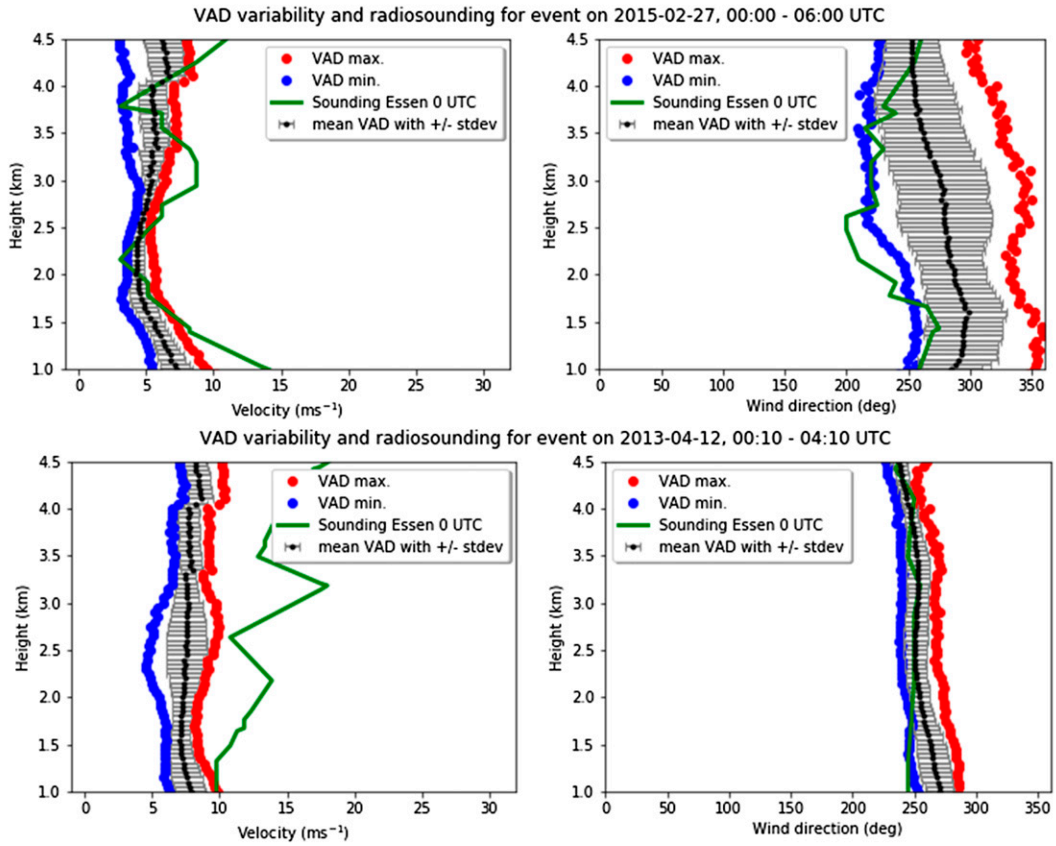

FIG. 14. VAD-derived wind profiles, their variability, and radiosoundings for precipitation events observed on (top) 27 Feb 2015 and (bottom) 12 Apr 2013 as exemplary cases with low ($r \approx 0.4$) or high ($r \approx 0.8$) correlations, respectively, between K_{DP} in the DGL and Z_H at the estimated advected surface location. Shown are average VAD-based wind (left) speed and (right) direction profiles (black lines), including minimum (blue dots) and maximum (red dots) values for all height levels observed during the events, together with the standard deviation intervals (gray bars). The profiles measured with the nearest available radiosounding in space and time (Essen at 0000 UTC for both events) are shown for comparison (green lines).

and the previous event (12 April 2013) may well be artifacts of the periodicity of the K_{DP} signatures (see Fig. 1).

Only 19 of the 27 long-lasting events (>3.5 h) show an increase in r when taking advection with radar-derived wind fields into account (see Table 1), which might be caused by changing wind conditions, among others, and thus deviations from the average wind profile during the precipitation events.

In the analyses presented in Table 1, a significant impact of K_{DP} in the DGL on the forthcoming surface precipitation is assumed regardless of their magnitudes; that is, the suggested nowcasting method has been applied to all long-lasting rain events. However, maybe only the most pronounced signatures, in excess of certain thresholds to be determined, provide exploitable nowcasting information with high correlations between K_{DP} in the DGL and surface rainfall at the estimated location. Attenuation effects have been neglected in these moderate stratiform events, but in single cases embedded convection cores may result in significant attenuation in Z_H(sfc) and impact the correlation analysis.

7. Summary and conclusions

The QVP method has been exploited to derive statistics of vertical profiles of polarimetric variables for 52 stratiform events lasting from 1 h 25 min to 12 h 35 min observed with the polarimetric X-band radar BoXPol in Bonn. The slant range of azimuthally averaged PPIs measured at 18° elevation angle with 100 m radial resolution was transformed into height and provided low-noise quasi-vertical profiles with a vertical resolution decreasing with height due to beam broadening of 100 m at 2-km height and 270 m at 5-km height. This dataset allows for a reliable estimation of intrinsic polarimetric properties of the melting layer and the

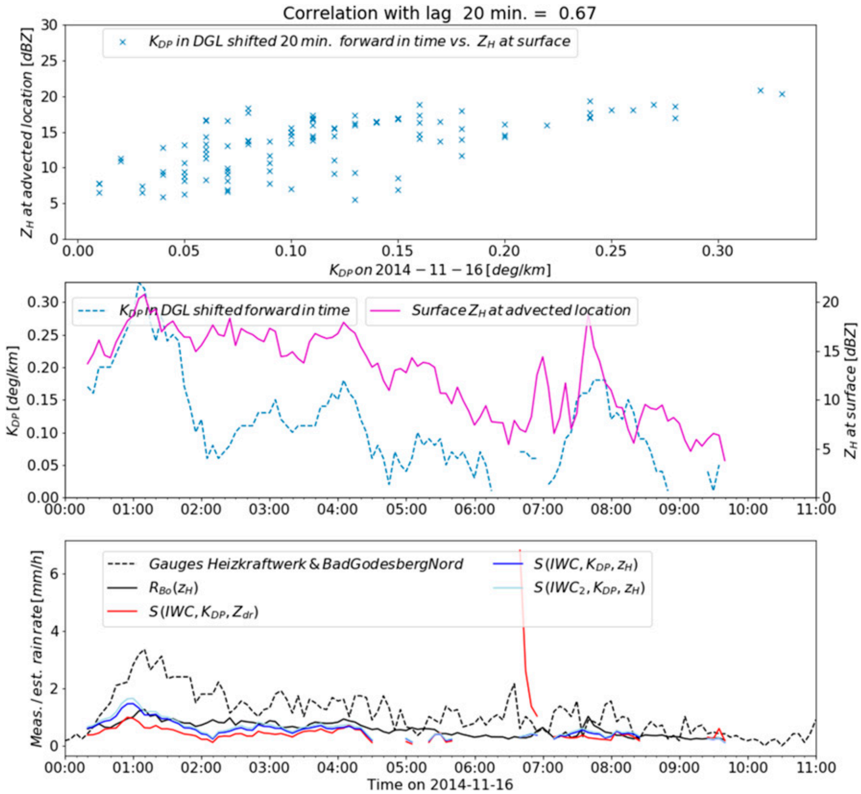

FIG. 15. (top) Scatterplot of K_{DP} in the DGL against Z_H at predicted surface location 20 min later, exploiting VADs, (middle) the corresponding time series of surface Z_H and K_{DP} in the DGL shifted forward in time, and (bottom) the $R_{\mathrm{Bo}}(Z_H)$-derived [Eq. (18)] and measured rain rates 20 min later at the closest rain gauges (Heizkraftwerk and Bad Godesberg Nord) together with three S(IWC) retrievals using Eqs. (3), (16) and (17), respectively, for the low-wind precipitation event observed on 16 Nov 2014.

dendritic growth layer, on which an in-depth evaluation of numerical atmospheric models and an exploitation of DGL signatures for nowcasting of precipitation enhancement can be based.

The derived DGL statistics reveals similarities and also significant differences with results from other regions. In agreement with the study by Griffin et al. (2018) performed in the United States, we find a positive correlation between K_{DP} and Z_H in the DGL; probably because of our low values of Z_{DR}, a negative correlation between Z_{DR} and Z_H could not be confirmed. Studies performed by Bechini et al. (2013) in Italy or Schneebeli et al. (2013) in the eastern Swiss Alps also showed only moderate Z_{DR} values, which may point toward climatological differences between Europe and the United States.

Kennedy and Rutledge (2011), Bechini et al. (2013) and Trömel et al. (2017), among others, suggested nowcasting of imminent precipitation enhancement based on K_{DP} bands and Z_H gradients in the DGL, which signal an increased ice crystal number concentration and intense aggregation. Surface precipitation enhancement can be expected after the time needed for the snowflakes (or raindrops after passing the melting layer) to reach the ground. The identification and quantification of snow generated in the DGL requires, however, the azimuthal averaging inherent to the QVP method; it cannot be based, for example, on 3D composites because the signal is often much too noisy. In this study, lagged correlations between K_{DP} in the DGL and Z_H near the surface have been calculated taking trajectories of the snow generated in the DGL to the ground into account. Wind profiles from both the nearest radiosoundings and VADs have been used to estimate the location of potential successive surface precipitation enhancement, and lagged correlation analyses have been performed to determine the related lead times. Since radiosoundings are sparse in time and space, the VAD technique, providing wind profiles at the radar location with 5 min temporal resolution, has been identified as more suitable for the nowcasting application leading on average to higher correlations between K_{DP} in the DGL

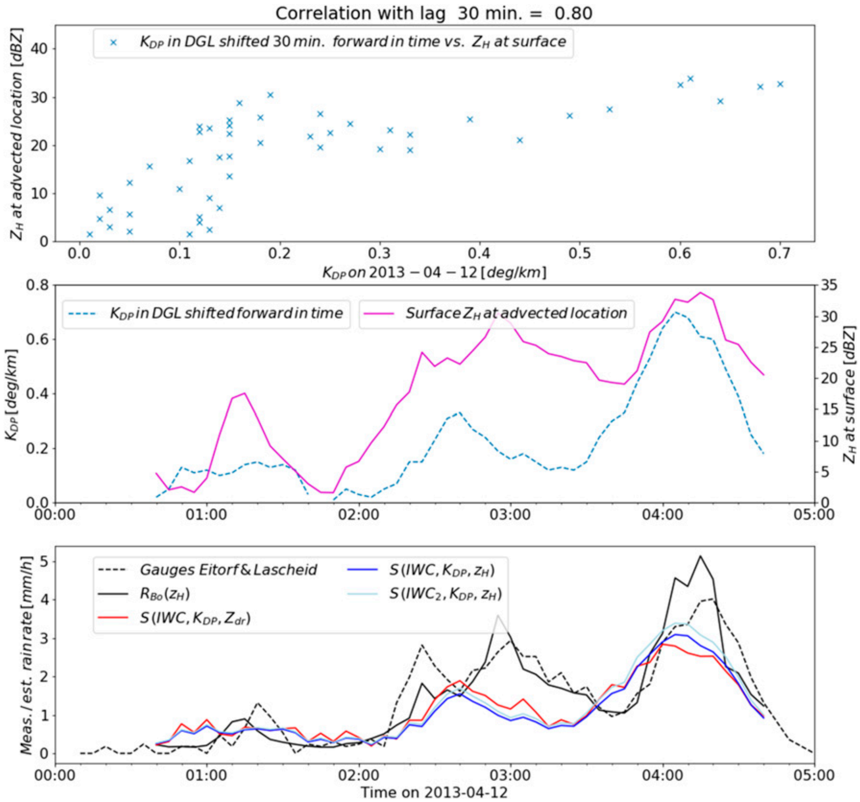

FIG. 16. As in Fig. 15, but for the precipitation event observed on 12 Apr 2013.

and Z_H near the surface. Also, a tendency for higher correlations between K_{DP}(DGL) and Z_H(sfc) in environmental conditions with low winds, small advected distances, and small variability in wind direction is observed.

Surface rain rates at the expected locations and times have been estimated using polarimetric retrievals of the ice water content IWC (Bukovčić et al. 2018; Ryzhkov et al. 2018) and the related snow water equivalent precipitation rate S(IWC). The comparison with both surface-reflectivity-derived and gauge-observed rain rates showed good agreement. However, error estimates of the polarimetric IWC retrievals are still sparse. So far, Ryzhkov et al. (1998) compared in situ observations with IWC(Z_H), IWC(K_{DP}), and IWC(K_{DP}, Z_{dr}) retrievals during the VORTEX experiment in Oklahoma and obtained clear improvements using polarimetry; the additional use of Z_{dr} slightly improved the agreement between the IWC(K_{DP}) retrievals and the observations. Other evaluation attempts using airborne X-band polarimetric radar and in situ aircraft measurements have been made by Nguyen et al. (2017, 2019). Analysis of data collected in the ice regions of tropical convective clouds during 7 flights indicates that the IWC(K_{DP}, Z_{dr}), Eq. (3), yields a root-mean-square error of the IWC estimate of 0.49 g m^{-3} with the bias within 6%. Because of the unknown details of the development of S(IWC) including accretion, riming, and evaporation along the precipitation trajectories from the DGL down to the surface, only correlations with measured surface rain rates can be expected, and we can claim only these at this stage. While we expect changes in the DGL to translate into changes of precipitation rates at the surface—as the correlations suggest—no conclusions regarding biases in surface precipitation estimates based on the polarimetric S(IWC) retrievals in the DGL can be drawn at the moment. Climatological vertical profiles of snow water equivalent precipitation rates S categorized with respect to the synoptic and environmental conditions are required to estimate the impact of microphysical processes on S(IWC) along the precipitation trajectories and to project the measurements in the DGL to the surface. The inclusion of microphysical fingerprints (e.g., Kumjian 2012; Xie et al. 2016) to detect the dominant microphysical processes affecting precipitation along its fall streak (e.g., depositional growth/sublimation, aggregation, and riming) appears to be a promising strategy to derive the climatological profiles.

Potential operational nowcasting applications of QVPs may experience problems with capturing isolated cores of

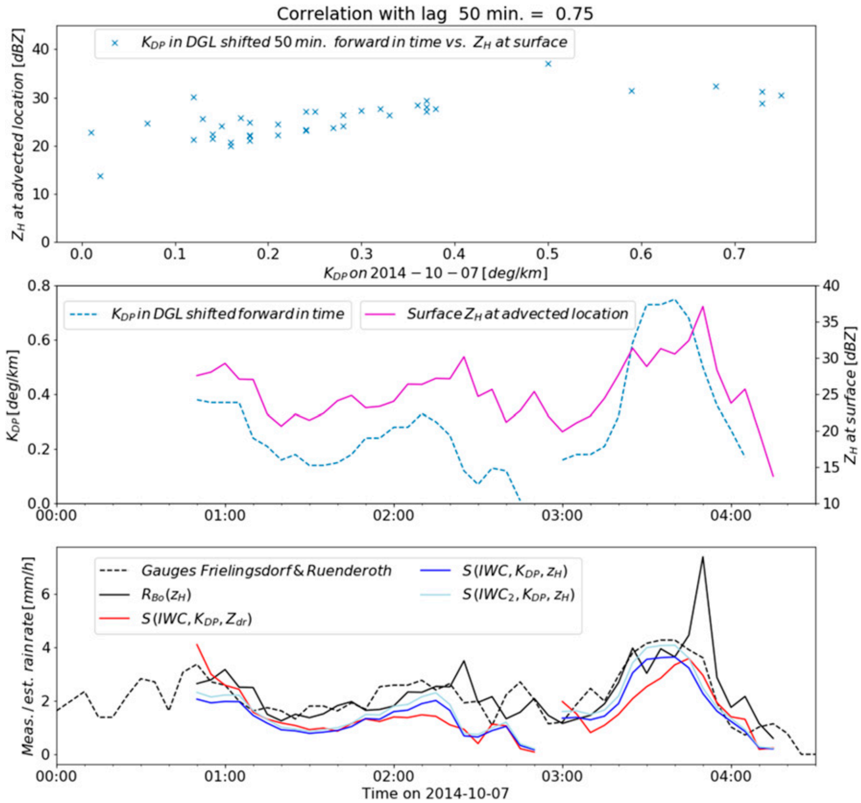

FIG. 17. As in Figs. 15, but for the precipitation event observed on 7 Oct 2014. Respective QVPs are shown in Fig. 1.

snow aloft. The azimuthal averaging in QVPs results in different horizontal resolutions between the DGL and the surface so that spatially isolated signatures of snow enhancement far from the radar may not be detected at all. The expanded QVP methodology by Tobin and Kumjian (2017) or the columnar vertical profile (CVP) method suggested by Murphy et al. (2017) may overcome some deficiencies of the initial QVP technique, because the CVP processing implies averaging data within a prescribed sector in range and azimuth and over multiple radar elevation scans. Hence, CVPs can be calculated at any location within the radar range. Figure 18 shows the radar-centric QVP time series with CVP time series for sectors northeast (azimuths 40°–60°; range 20–40 km) and southwest (azimuths 220°–240°; range 20–40 km) of BoXPol for the precipitation event on 12 April 2013 (Fig. 16). Pronounced differences in the temporal evolution and magnitudes of K_{DP} are visible in the three products. Hence, we propose to detect respective DGL signatures using several CVPs within the radar range and the calculation of hydrometeor trajectories to the surface utilizing wind information from the VAD technique, or numerical weather prediction (NWP) models.

The combined use of QVPs with a melting-layer detection strategy allows to reliably estimate Z_H, Z_{DR}, and ρ_{HV} and also to separate K_{DP} and δ in the ML. Our confidence in the δ-K_{DP} decomposition is supported by a high correlation between K_{DP}(ML) and the measured rain rate at the surface (r = 0.65; Fig. 8), moderate correlation between K_{DP}(ML) and Z_H(ML) (r = 0.51; Fig. 7), and moderate correlation between Z_{DR}(ML) and δ(ML) (r = 0.51, not shown). However, the K_{DP} estimation proposed by Trömel et al. (2013, 2014) assumes a constant K_{DP} within the ML and thus provides only an estimate of the average instead of the vertical profile of K_{DP}. It represents just one possible strategy and there is a chance that other algorithms (so far restricted to estimate K_{DP} in rain while maintaining its spatial variability) will be modified for its application to the ML in the future (e.g., Reinoso-Rondinel et al. 2018). K_{DP} in the ML—as retrieved here—is well correlated with the near-surface rain rate and also with the cooling rate by melting/ sublimation in the ML (Carlin 2018). We believe that the utilization of the K_{DP} measurements in the DGL and ML can also help the modelers to refine microphysical parameterization schemes; K_{DP} is a lower moment of the snow size distribution than Z_H, and

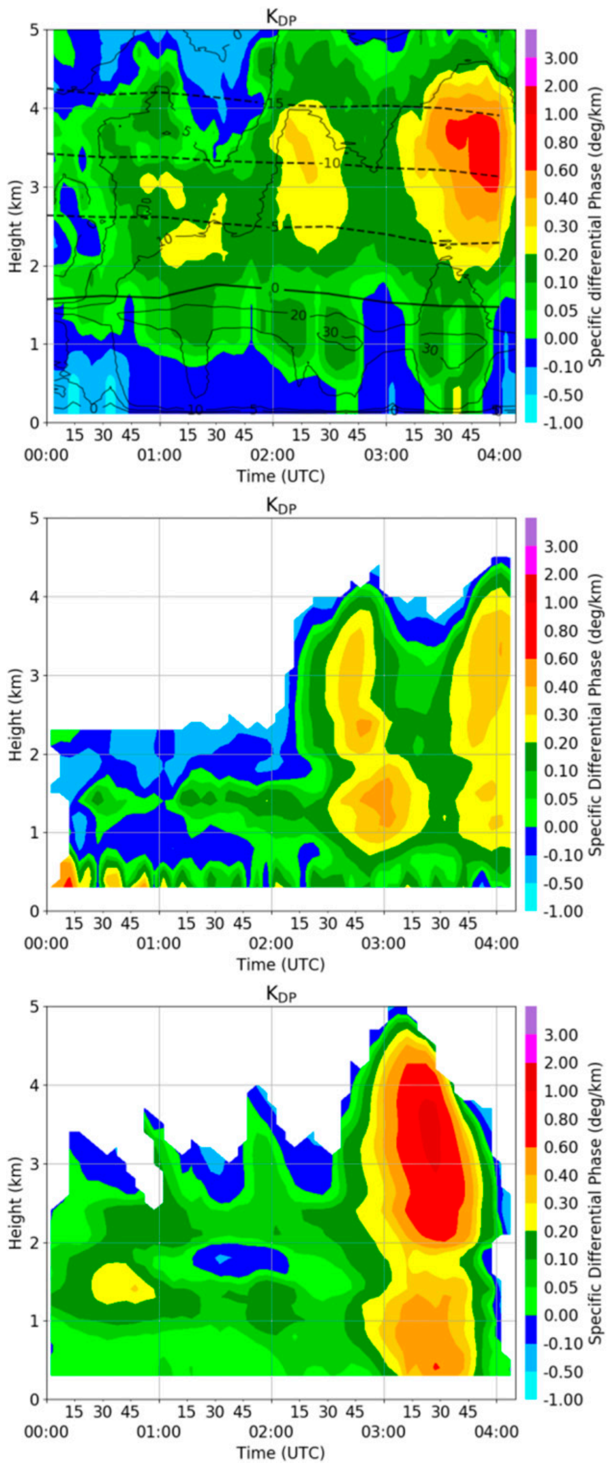

FIG. 18. Comparison of the QVP of K_{DP} (top) centered over BoXPol for the precipitation event observed on 12 Apr 2013 with the CVPs for sectors (middle) northeast of BoXPol (azimuths 40°–60° and range 20–40 km) and (bottom) southwest of BoXPol (azimuths 220°–240° and range 20–40 km).

therefore it is better suited for quantification of IWC and mean volume diameter.

The BoXPol statistics of polarimetric variables in the ML are well in line with the magnitudes observed in Davos (Swiss Alps) by Wolfensberger et al. (2016). Our empirical distribution of X band δ(ML) supports earlier studies by Trömel et al. (2014) that were based on fewer observations—and shows considerably smaller values relative to C and S bands. Similar to Wolfensberger et al. (2016), the BoXPol statistics show increasing reflectivities in the ML [Z_H(ML)] with increasing ML thickness. A direct comparison, however, indicates a shift to deeper MLs for given Z_H(ML) in the Wolfensberger et al. (2016) study, which may be explainable with regional differences or the restriction of the Bonn statistics to relatively low rain rates.

The Bonn vertical profiles of Z_H below the ML suggest impacts of evaporation; its value at the surface, Z_H(sfc), is on average 2.2 dB smaller than directly below the ML, Z_H(rain). This result differs from the study by Fabry and Zawadzki (1995), who assumed a constant Z_H below the ML based on X-band statistics performed at the J. S. Marshall Radar Observatory (MRO) in Sainte-Anne-de-Bellevue in Quebec. As for the DGL, we suspect climatological differences in the atmospheric moisture to be responsible. In agreement with theoretical studies by Kumjian and Ryzhkov (2010) and Xie et al. (2016), the Z_{DR} profile below the ML is almost insensitive to evaporation.

Acknowledgments. The research of B. Hickman was carried out in the framework of the Extramural Research Program; this research network between universities, research institutes, and the Deutscher Wetterdienst (DWD) is funded by the BMVBS (Federal Ministry of Transport, Building and Urban Development). X-band weather radar data were provided by the Transregional Collaborative Research Center 32 (TR32; Simmer et al. 2015). Alexander Ryzhkov was supported with funding from NOAA–University of Oklahoma Cooperative Agreement NA11OAR4320072 under the U.S. Department of Commerce and from the National Science Foundation (Grant AGS-1143948).

REFERENCES

Andrić, J., M. R. Kumjian, D. Zrnić, J. M. Straka, and V. M. Melnikov, 2013: Polarimetric signatures above the melting layer in winter storms: An observational and modeling study. *J. Appl. Meteor. Climatol.*, **52**, 682–700, https://doi.org/10.1175/JAMC-D-12-028.1.

Baldauf, M., A. Seifert, J. Förstner, D. Majewski, M. Raschendorfer, and T. Reinhardt, 2011: Operational convective-scale numerical weather prediction with the COSMO Model: Description and sensitivities. *Mon. Wea. Rev.*, **139**, 3887–3905, https://doi.org/10.1175/MWR-D-10-05013.1.

Baldini, L., and E. Gorgucci, 2006: Identification of the melting layer through dual-polarization radar measurements at vertical incidence. *J. Atmos. Oceanic Technol.*, **23**, 829–839, https://doi.org/10.1175/JTECH1884.1.

Bandera, J., A. D. Papatsoris, P. A. Watson, J. Tan, and J. W. Goddard, 1998: Method for detecting the extend of the melting layer. *IET Electron. Lett.*, **34**, 2104–2105, https://doi.org/10.1049/el:19981462.

Bechini, R., L. Baldini, and V. Chandrasekar, 2013: Polarimetric radar observations in the ice region of precipitating clouds at C-band and X-band radar frequencies. *J. Appl. Meteor. Climatol.*, **52**, 1147–1169, https://doi.org/10.1175/JAMC-D-12-055.1.

Bellon, A., G. Lee, and I. Zawadzki, 2005: Error statistics of VPR corrections in stratiform precipitation. *J. Appl. Meteor.*, **44**, 998–1015, https://doi.org/10.1175/JAM2253.1.

Borowska, L., D. Zrnić, A. Ryzhkov, P. Zhang, and C. Simmer, 2011: Polarimetric estimates of a one month accumulation of light rain with a 3-cm wavelength radar. *J. Hydrometeor.*, **12**, 1024–1039, https://doi.org/10.1175/2011JHM1339.1.

Browning, K. A., and R. Wexler, 1968: The determination of kinematic properties of a wind field using Doppler radar. *J. Appl. Meteor.*, **7**, 105–113, https://doi.org/10.1175/1520-0450(1968)007<0105:TDOKPO>2.0.CO;2.

Bukovčić, P., A. Ryzhkov, D. Zrnić, and G. Zhang, 2018: Polarimetric radar relations for quantification of snow based on disdrometer data. *J. Appl. Meteor. Climatol.*, **57**, 103–120, https://doi.org/10.1175/JAMC-D-17-0090.1.

Carlin, J., 2018: The use of polarimetric radar data for informing numerical weather prediction models. Ph.D. thesis, University of Oklahoma, 252 pp.

——, and A. V. Ryzhkov, 2017: Polarimetric thermodynamic retrievals in the melting layer: One-dimensional spectral bin model simulations. *38th Conf. on Radar Meteorology*, Chicago, IL, Amer. Meteor. Soc., 99, https://ams.confex.com/ams/38RADAR/webprogram/Manuscript/Paper320676/Extended%20Abstract.pdf.

——, and ——, 2019: Estimation of melting-layer cooling rate from dual-polarization radar: Spectral bin model simulations. *J. Appl. Meteor. Climatol.*, **58**, 1485–1508, https://doi.org/10.1175/JAMC-D-18-0343.1.

Diederich, M., A. Ryzhkov, C. Simmer, P. Zhang, and S. Trömel, 2015a: Use of specific attenuation for rainfall measurement at X-band radar wavelengths. Part I: Radar calibration and partial beam blockage estimation. *J. Hydrometeor.*, **16**, 487–502, https://doi.org/10.1175/JHM-D-14-0066.1.

——, ——, ——, ——, and ——, 2015b: Use of specific attenuation for rainfall measurement at X-band radar wavelengths. Part II: Rainfall estimates and comparison with rain gauges. *J. Hydrometeor.*, **16**, 503–516, https://doi.org/10.1175/JHM-D-14-0067.1.

Doms, G., and U. Schättler, 2002: A description of the non-hydrostatic regional model LM, Part I: Dynamics and numerics. *COSMO Newsletter*, No. 2, Consortium for Small-Scale Modeling, Offenbach, Germany, 225–235.

Fabry, F., and I. Zawadzki, 1995: Long-term radar observations of the melting layer of precipitation and their interpretation. *J. Atmos. Sci.*, **52**, 838–851, https://doi.org/10.1175/1520-0469(1995)052<0838:LTROOT>2.0.CO;2.

Giangrande, S. E., J. M. Krause, and A. V. Ryzhkov, 2008: Automatic designation of the melting layer with a polarimetric prototype of the WSR-88D radar. *J. Appl. Meteor. Climatol.*, **47**, 1354–1364, https://doi.org/10.1175/2007JAMC1634.1.

Grazioli, J., M. Schneebeli, and A. Berne, 2014: Accuracy of phase-based algorithms for the estimation of the specific differential phase shift using simulated polarimetric weather radar data. *IEEE Geosci. Remote Sens. Lett.*, **11**, 763–767, https://doi.org/10.1109/LGRS.2013.2278620.

Griffin, E., T. Schuur, and A. Ryzhkov, 2018: A polarimetric analysis of ice microphysical processes in snow using quasi-vertical profiles. *J. Appl. Meteor. Climatol.*, **57**, 31–50, https://doi.org/10.1175/JAMC-D-17-0033.1.

Heistermann, M., S. Jacobi, and T. Pfaff, 2013: Technical Note: An open source library for processing weather radar data (wradlib). *Hydrol. Earth Syst. Sci.*, **17**, 863–871, https://doi.org/10.5194/hess-17-863-2013.

Hobbs, P. V., and A. L. Rangno, 1985: Ice particle concentrations in clouds. *J. Atmos. Sci.*, **42**, 2523–2549, https://doi.org/10.1175/1520-0469(1985)042<2523:IPCIC>2.0.CO;2.

Hogan, R. J., M. P. Mittermaier, and A. J. Illingworth, 2006: The retrieval of ice water content from radar reflectivity factor and temperature and its use in evaluating a mesoscale model. *J. Appl. Meteor. Climatol.*, **45**, 301–317, https://doi.org/10.1175/JAM2340.1.

Hou, T., H. Lei, Z. Hu, and J. Zhou, 2014: Aircraft observations of ice particle properties in stratiform precipitating clouds. *Adv. Meteor.*, **2014**, 206352, https://doi.org/10.1155/2014/206352.

Kennedy, P. C., and S. A. Rutledge, 2011: S-band dual-polarization radar observations of winter storms. *J. Appl. Meteor. Climatol.*, **50**, 844–858, https://doi.org/10.1175/2010JAMC2558.1.

Khain, A., A. Pokrovsky, D. Rosenfeld, U. Blahak, and A. Ryzhkov, 2011: The role of CCN in precipitation and hail in a midlatitude storm as seen in simulations using a spectral (bin) microphysics model in a 2D dynamic frame. *Atmos. Res.*, **99**, 129–146, https://doi.org/10.1016/j.atmosres.2010.09.015.

——, V. Phillips, N. Benmoshe, and A. Pokrovsky, 2012: The role of small soluble aerosols in the microphysics of deep maritime clouds. *J. Atmos. Sci.*, **69**, 2787–2807, https://doi.org/10.1175/2011JAS3649.1.

Kumjian, M. R., 2012: The impact of precipitation physical processes on the polarimetric radar variables. Ph.D. dissertation, University of Oklahoma, 327 pp.

——, and A. V. Ryzhkov, 2010: The impact of evaporation on polarimetric characteristics of rain: Theoretical model and practical implications. *J. Appl. Meteor. Climatol.*, **49**, 1247–1267, https://doi.org/10.1175/2010JAMC2243.1.

——, ——, H. D. Reeves, and T. J. Schuur, 2013: A dual-polarization radar signature of hydrometeor refreezing in winter storms. *J. Appl. Meteor. Climatol.*, **52**, 2549–2566, https://doi.org/10.1175/JAMC-D-12-0311.1.

——, A. P. Khain, N. Benmoshe, E. Ilotoviz, A. V. Ryzhkov, and V. T. J. Phillips, 2014: The anatomy and physics of ZDR columns: Investigating a polarimetric radar signature with a spectral bin microphysical model. *J. Appl. Meteor. Climatol.*, **53**, 1820–1843, https://doi.org/10.1175/JAMC-D-13-0354.1.

——, S. Mishra, S. Giangrande, T. Toto, A. Ryzhkov, and A. Bansemer, 2016: Polarimetric radar and aircraft observations of saggy bright band during MC3E. *J. Geophys. Res. Atmos.*, **121**, 3584–3607, https://doi.org/10.1002/2015JD024446.

Lauri, T., J. Koistinen, and D. Moisseev, 2012: Advection-based adjustment of radar measurements. *Mon. Wea. Rev.*, **140**, 1014–1022, https://doi.org/10.1175/MWR-D-11-00045.1.

Löhnert, U., and Coauthors, 2015: JOYCE: Jülich Observatory for Cloud Evolution. *Bull. Amer. Meteor. Soc.*, **96**, 1157–1174, https://doi.org/10.1175/BAMS-D-14-00105.1.

Matrosov, S., K. Clark, and D. Kingsmill, 2007: A polarimetric radar approach to identify rain, melting layer, and snow regions for applying corrections to vertical profiles of reflectivity. *J. Appl. Meteor. Climatol.*, **46**, 154–166, https://doi.org/10.1175/JAM2508.1.

——, C. Campbell, D. Kingsmill, and E. Sukovich, 2009: Assessing snowfall rates from X-band radar reflectivity measurements. *J. Atmos. Oceanic Technol.*, **26**, 2324–2339, https://doi.org/10.1175/2009JTECHA1238.1.

Moisseev, D. N., S. Lautaportti, J. Tyynela, and S. Lim, 2015: Dual-polarization radar signatures in snowstorms: Role of snowflake aggregation. *J. Geophys. Res. Atmos.*, **120**, 12 644–12 655, https://doi.org/10.1002/2015JD023884.

Murphy, A., A. Ryzhkov, P. Zhang, G. McFarquhar, W. Wu, and D. Stechman, 2017: A polarimetric and microphysical analysis of the stratiform rain region of MCSs. *38th Conf. on Radar Meteorology*, Chicago, IL, Amer. Meteor. Soc., 682, https://ams.confex.com/ams/98Annual/webprogram/Paper334391.html.

Nguyen, C., M. Wolde, K. Baibakov, and A. Korolev, 2017: Detection and estimation of high ice water content using X- and W-band dual-polarization airborne radar data. *38th Conf. on Radar Meteorology*, Chicago, IL, Amer. Meteor. Soc., 89, https://ams.confex.com/ams/38RADAR/webprogram/Paper321101.html.

Nguyen, C. M., M. Wolde, and A. Korolev, 2019: Determination of ice water content (IWC) in tropical convective clouds from X-band dual-polarization airborne radar. *Atmos. Meas. Tech.*, **12**, 5897–5911, https://doi.org/10.5194/amt-12-5897-2019.

Reinoso-Rondinel, R., C. Unal, and H. Russchenberg, 2018: Adaptive and high-resolution estimation of specific differential phase for polarimetric X-band weather radars. *J. Atmos. Oceanic Technol.*, **35**, 555–573, https://doi.org/10.1175/JTECH-D-17-0105.1.

Ryzhkov, A., and D. Zrnić, 2019: *Radar Polarimetry for Weather Observations*. Springer Atmospheric Sciences, 486 pp.

——, ——, and B. A. Gordon, 1998: Polarimetric method for ice water content determination. *J. Appl. Meteor.*, **37**, 125–134, https://doi.org/10.1175/1520-0450(1998)037<0125:PMFIWC>2.0.CO;2.

——, H. Reeves, J. Krause, and H. Burcham, 2014: Discrimination between winter precipitation types based on explicit microhysical modeling of melting and refreeezing in the polarimetric hydrometeor classification algorithm. *Eighth European Conf. on Radar Meteorology*, Garmisch-Partenkirchen, Germany, European Meteorological Society, MIC.P07, http://www.pa.op.dlr.de/erad2014/programme/ExtendedAbstracts/198_Ryzhkov.pdf.

——, P. Zhang, H. Reeves, M. Kumjian, T. Tschallener, S. Trömel, and C. Simmer, 2016: Quasi-vertical profiles—A new way to look at polarimetric radar data. *J. Atmos. Oceanic Technol.*, **33**, 551–562, https://doi.org/10.1175/JTECH-D-15-0020.1.

——, P. Bukovčić, A. Murphy, P. Zhang, and G. McFarquhar, 2018: Ice microphysical retrievals using polarimetric radar data. *Proc. 10th European Conf. on Radar in Meteorology and Hydrology*, Ede-Wageningen, Netherlands, 40, projects.knmi.nl/erad2018/ERAD2018_extended_abstract_040.pdf.

Schneebeli, M., N. Dawes, M. Lehning, and A. Berne, 2013: High-resolution vertical profiles of X-band polarimetric radar observables during snowfall in the Swiss Alps. *J. Appl. Meteor. Climatol.*, **52**, 378–394, https://doi.org/10.1175/JAMC-D-12-015.1.

——, J. Grazioli, and A. Berne, 2014: Improved estimation of the specific differential phase shift using a compilation of Kalman filter ensembles. *IEEE Trans. Geosci. Remote Sens.*, **52**, 5137–5149, https://doi.org/10.1109/TGRS.2013.2287017.

Schrom, R. S., M. R. Kumjian, and Y. Lu, 2015: Polarimetric radar signatures of dendritic growth zones within Colorado winter storms. *J. Appl. Meteor. Climatol.*, **54**, 2365–2388, https://doi.org/10.1175/JAMC-D-15-0004.1.

Simmer, C., and Coauthors, 2015: Monitoring and modeling the terrestrial system from pores to catchments: The transregional collaborative research center on patterns in the soil–vegetation–atmosphere system. *Bull. Amer. Meteor. Soc.*, **96**, 1765–1787, https://doi.org/10.1175/BAMS-D-13-00134.1.

Smyth, T. J., and A. J. Illingworth, 1998: Radar estimates of rainfall rates at the ground in bright band and non-bright band events. *Quart. J. Roy. Meteor. Soc.*, **124**, 2417–2434, https://doi.org/10.1002/qj.49712455112.

Steiner, M., R. Houze, and S. Yuter, 1995: Climatological characterization of three-dimensional storm structure from operational radar and rain gauge data. *J. Appl. Meteor.*, **34**, 1978–2007, https://doi.org/10.1175/1520-0450(1995)034<1978:CCOTDS>2.0.CO;2.

Takahashi, T., Endoh, G. Wakahama, and N. Fukuta, 1991: Vapor diffusional growth of free-falling snow crystals between −3 and −23°C. *J. Meteor. Soc. Japan*, **69**, 15–30, https://doi.org/10.2151/jmsj1965.69.1_15.

Tobin, D., and M. Kumjian, 2017: Polarimetric radar and surface-based precipitation-type observations of ice pellet to freezing rain transitions. *Wea. Forecasting*, **32**, 2065–2082, https://doi.org/10.1175/WAF-D-17-0054.1.

Trömel, S., M. R. Kumjian, A. V. Ryzhkov, C. Simmer, and M. Diederich, 2013: Backscatter differential phase—Estimation and variability. *J. Appl. Meteor. Climatol.*, **52**, 2529–2548, https://doi.org/10.1175/JAMC-D-13-0124.1.

——, A. Ryzhkov, P. Zhang, and C. Simmer, 2014: Investigations of backscatter differential phase in the melting layer. *J. Appl. Meteor. Climatol.*, **53**, 2344–2359, https://doi.org/10.1175/JAMC-D-14-0050.1.

——, ——, and C. Simmer, 2017: Climatology of the vertical profiles of polarimetric radar variables at X band in stratiform clouds. *38th Conf. on Radar Meteorology*, Chicago, IL, Amer. Meteor. Soc., 5, https://ams.confex.com/ams/38RADAR/webprogram/Manuscript/Paper320485/ExtAbstract_Troemel_AMS_Radar2017.pdf.

——, J. Quaas, S. Crewell, A. Bott, and C. Simmer, 2018: Polarimetric radar observations meet atmospheric modelling. *Proc. 19th Int. Radar Symp.*, Bonn, Germany, IEEE, https://doi.org/10.23919/IRS.2018.8448121.

Vignal, B., and W. Krajewski, 2001: Large-sample evaluation of two methods to correct range-dependent error for WSR-88D rainfall estimates. *J. Hydrometeor.*, **2**, 490–504, https://doi.org/10.1175/1525-7541(2001)002<0490:LSEOTM>2.0.CO;2.

Vogel, J. M., and F. Fabry, 2018: Contrasting polarimetric observations of stratiform riming and nonriming events. *J. Appl. Meteor. Climatol.*, **57**, 457–476, https://doi.org/10.1175/JAMC-D-16-0370.1.

Vulpiani, G., M. Montopoli, L. Delli Passeri, A. G. Gioia, P. Giordano, and F. S. Marzano, 2012: On the use of dual-polarized C-band radar for operational rainfall retrieval in mountainous areas. *J. Appl. Meteor. Climatol.*, **51**, 405–425, https://doi.org/10.1175/JAMC-D-10-05024.1.

White, A. B., D. J. Gottas, E. T. Strem, F. M. Ralph, and P. J. Neiman, 2002: An automated brightband height detection algorithm for use with Doppler radar spectral moments. *J. Atmos. Oceanic Technol.*, **19**, 687–697, https://doi.org/10.1175/1520-0426(2002)019<0687:AABHDA>2.0.CO;2.

Williams, E., and Coauthors, 2015: Measurements of differential reflectivity in snowstorms and warm season stratiform systems. *J. Appl. Meteor. Climatol.*, **54**, 573–595, https://doi.org/10.1175/JAMC-D-14-0020.1.

Wolfensberger, D., D. Scipion, and A. Berne, 2016: Detection and characterization of the melting layer based on polarimetric radar scans. *Quart. J. Roy. Meteor. Soc.*, **142**, 108–124, https://doi.org/10.1002/qj.2672.

Xie, X., R. Evaristo, S. Trömel, P. Saavedra, C. Simmer, and A. Ryzhkov, 2016: Radar observation of evaporation and implications for quantitative precipitation and cooling rate estimation. *J. Atmos. Oceanic Technol.*, **33**, 1779–1792, https://doi.org/10.1175/JTECH-D-15-0244.1.